**1**    **A systematic comparison of experimental set-ups for modelling extensional tectonics**

**3**      Frank Zwaan[a,b], Guido Schreurs[a], Susanne J.H. Buiter[c,d],

**5**   a) Institute of Geological Sciences, University of Bern, Baltzerstrasse 1+3, CH-3012 Bern, Switzerland
**6**   b) Current affiliation: Dipartimento di Scienze della Terra, Università degli Studi di Firenze, Via La Pira, 4, 50121 Florence, Italy
**7**   c) Team for Solid Earth Geology, Geological Survey of Norway (NGU), Leiv Eirikssons vei 39, 7040 Trondheim, Norway
**8**   d) The Centre for Earth Evolution and Dynamics, University of Oslo, Sem Sælands vei 2A, 0371 Oslo, Norway

**11**   **Abstract**

**13**   Analogue modellers investigating extensional tectonics often use different machines, set-ups
**14**   and model materials, so that direct comparisons of results from different studies can be
**15**   challenging. Here we present a systematic comparison of crustal-scale analogue experiments
**16**   using simple set-ups simulating extensional tectonics, involving either a foam base, a rubber
**17**   base, rigid basal plates or a conveyor base to deform overlying brittle-only or brittle-viscous
**18**   models. We use X-ray computed tomography (CT) techniques for a detailed 3D analysis of
**19**   internal and external model evolution.

**21**   We find that our brittle-only experiments are strongly affected by the specific set-up, as the
**22**   materials are directly coupled to the model base. Experiments with a foam or rubber base
**23**   undergo distributed faulting, whereas experiments with a rigid plate or conveyor base
**24**   experience localized deformation and the development of discrete rift basins. Pervasive
**25**   boundary effects may occur due to extension-perpendicular contraction of a rubber base.
**26**   Brittle-viscous experiments are less affected by the experimental setup than their brittle-only
**27**   equivalents as the viscous layer acts as a buffer that decouples the brittle layer from the base.
**28**   Brittle-viscous plate base and conveyor base experiments only localize deformation with high
**29**   brittle-to-viscous thickness ratios that increases brittle-viscous coupling. This effect is further
**30**   enhanced by higher strain rates.

**32**   Our set-ups are most appropriate for investigating crustal-scale extension in continental and
**33**   selected oceanic settings. Specific combinations of set-up and model materials may be used
**34**   for studying young or old regions, or wide or narrow extension. Here, natural factors as
**35**   temperature variations, extension rate, water content and lithology should be carefully
**36**   considered. We hope that our experimental overviews may serve as a guide for future
**37**   experimental studies of extensional tectonics.

**41**   **1. Introduction**

**43**   1.1 Analogue experimental set-ups for investigating extensional tectonics

**45**   Tectonic analogue modellers have historically used different experimental apparatus and model
**46**   materials to investigate continental extension. These experiments have provided the scientific
**47**   community with highly valuable insights in the evolution of basins and initial rift structures.
**48**   However, a robust comparison between various experiments is challenging, because of the
**49**   variety of experimental set-ups and model materials that have been used. Experiments have,
**50**   for example, used set-ups involving (a combination of) basal foam bars, basal rubber sheet,
**51**   rigid basal plates or conveyor belt style basal sheets with moving sidewalls to deform model
**52**   materials (e.g. Allemand et al. 1989; Acocella et al. 1999; Bahroudi et al. 2003; Amilibia et al.
**53**   2005; Alonso-Henar et al. 2015; Philippon et al. 2015). Alternatively, extension can be achieved
**54**   through gravitational gliding or spreading, in which case no moving sidewalls or an extending
**55**   base needs to be applied (e.g. Gartrell 1997; Fort et al. 2004; Acocella et al. 2005). Analogue
**56**   materials used to simulate brittle parts of the lithosphere include, among others, quartz or
**57**   feldspar sand, silica flour, microbeads, and (kaolinite) clay (Hubbert 1951, Elmohandes 1981;
**58**   Serra & Nelson 1988; Clifton & Schlische 2001; Autin et al. 2010; Abdelmalak et al. 2016, Fig.

59    1). Pure silicone oils and silicone putties are frequently used as analogues for ductile parts of
60    the lithosphere (Basile & Brun 1999; Michon & Merle 2000; Sun et al. 2009, Fig. 1).
61
62    Vendeville et al. (1987) present experiments that highlight several factors controlling the
63    geometry of fault systems in extensional tectonics. The study used rubber sheet set-ups with a
64    brittle sand layer for homogeneous thin-skinned deformation, brittle-viscous gravity-spreading
65    models resting on a solid base, and experiments with the whole brittle-viscous lithospheric
66    analogue floating on a simulated asthenosphere (Fig. 1). The results provide a first impression
67    of the differences between these set-ups, revealing the correlation between fault spacing and
68    layer thickness in brittle materials, rift localisation in brittle-viscous settings and isostatic effects,
69    such as tilted margins due to the influence of an asthenosphere (Fig. 1). Yet the many
70    experimental parameters were widely different from experiment to experiment, making a
71    quantitative comparison difficult.
72
73    Allemand & Brun (1991) test the influence of material layering, but using a conveyor belt set-up
74    to achieve both symmetric and asymmetric extension with a velocity discontinuity (VD). The
75    basal sheets diverge, representing a fracture in the underlying (not-simulated) brittle
76    lithospheric mantle. Asymmetric extension is shown to generate strongly asymmetric rift
77    geometries, in both brittle and brittle-viscous models. The rifts under symmetric extension
78    conditions also develop a degree of structural asymmetry. Model parameters such as layer
79    thickness, material properties and extension velocities are however not clearly defined, again
80    making again a direct comparison of these experiments challenging.
81
82    Brun (1999) summarises extension experiments with a focus on layer rheology and extension
83    velocity. He shows that increasing extension velocities in crustal-scale brittle-viscous conveyor
84    belt models increase viscous strength and brittle-viscous coupling, favouring widespread
85    deformation or wide rifting. By contrast, low extension velocities lead to localized extension or
86    narrow rifting. A similar effect is obtained by changing the brittle-to-viscous thickness ratio: a
87    high ratio of 3:1 leads to high coupling and wide rifting, whereas a small ratio of 1:1 leads to low
88    coupling and narrow rifting. On a lithospheric scale however, the behaviour of the upper mantle
89    becomes important as well (Fig. 1); a single fracture in a strong upper mantle layer may induce
90    narrow deformation in the overlying crustal layers, whereas a weak upper mantle promotes
91    distributed deformation. The models also suggest that within such wide rifts, local weaknesses
92    can account for the development of core complexes. Next to providing a summarizing scheme
93    similar to Brun (1999), Corti et al. (2003) show how magma presence can control graben
94    initiation in narrow rifts and cause a wide rift to shift in core complex mode. The authors also
95    describe the additional effects of oblique extension and multiple extension phases on rift
96    evolution. However, the models presented in both review articles come from numerous studies
97    and are often performed with sometimes very different techniques and parameters.
98
99    The additional significance of VDs in the brittle upper mantle was investigated by Michon &
100   Merle (2000; 2003) by means of brittle-viscous base plate experiments, where the VD is
101   situated at the edge of the plate. A single VD leads to asymmetric extension and the
102   development of a single rift, whereas a double VD experiment may form two or more rift basins,
103   depending on the initial distance between the VDs. This is valid for high strain rates, as low
104   strain rates focus deformation (narrow rifting), decreasing the number of rift basins. Apart from
105   the varying strain rates and VDs, the other parameters such as model size, materials and layer
106   thickness remained fixed.
107
108   Schreurs et al. (2006) compared results of a brittle-viscous plate base extension experiment
109   that was run by five analogue laboratories. The overall experimental set-up was kept as similar
110   as possible using, for example, the same foil to cover the base of the apparatus, the same
111   extension velocity and the same viscous material (PDMS). But differences occurred in brittle
112   materials (different types of sand and a wet clay) and model width. This study illustrated the
113   overall large-scale structural similarities, but also showed differences in fault dip angle and fault
114   spacing, that were related to differences in model materials and/or model set-up.
115

### 1.2 Analogue materials used in extension experiments

Brittle, Mohr-Coulomb type materials have very similar internal friction angles with respect to their natural analogues (ranging between ca. 25° and 40°, Klinkmüller et al. 2016; Schellart & Strak 2016). Granular materials such as dry quartz sand have a very low cohesion and are considered a good analogue for large-scale models aiming at the whole brittle crust or the crust and lithospheric mantle (Fig. 1). By contrast, high-cohesion materials, such as silica flour and clay (C = 40-750 Pa, Eisenstadt & Sims 2005; Guerit et al. 2016), are better suitable for modelling the uppermost kilometres of the crust where cohesion is an important rheological factor. Intermediate cohesions can be obtained by mixing granular materials (Abdelmalak et al. 2016; Montanari et al. 2017). Low-friction microbeads allow the modelling of structural weaknesses or weak crustal lithologies (e.g. Colletta et al. 1991; Panien et al. 2005). The density of brittle analogue materials depends on the specific density, the grain size and handling techniques, as well as water content (for clays), but lies generally between ca. 1400-1800 kg/cm$^3$ (e.g. Krantz 1991; Eisenstadt & Sims 2005; Klinkmüller et al. 2016).

Pure silicone oils consist of polydimethylsiloxane (PDMS), are transparent, have a density of ca. 1000 kg/m$^3$ (Weijermars & Schmeling 1986) and a Newtonian viscosity between c. $10^3$ Pa·s and $10^5$ Pa·s at room temperature and at typical experimental deformation rates (Rudolf et al. 2015; Schellart & Strak 2016). Silicone putties are mixtures of polyborondimethylsiloxane (PBDMS) and inert fillers (Weijermars, 1986), and have higher densities than pure silicone oils. . Examples of opaque silicone putties commonly used in analogue modelling include Rhodorsil Gomme GS1R (Cobbold & Quinquis, 1980), Rhodorsil Silbione 70009 (Nalpas & Brun, 1993) and Dow Corning DC3179 (Dixon and Summers, 1985). Their density range varies between c. 1140 and 1420 kg/m$^3$ and they display Newtonian viscosities between c. $10^4$ and $4 \cdot 10^5$ Pa·s at room temperature (e.g., Casas et al., 2001; Cagnard et al., 2006; Konstantinovskaya et al., 2007). It should be noted that the viscosity of silicone-based materials can in some cases strongly depend on temperature (Cagnard et al. 2006) and also aging processes have an effect on silicone behaviour (Rudolf et al. 2015 and references therein). Pure silicone oils and silicone putties can be mixed with for instance sand or metallic powders to modify the material's density and viscosity (e.g. Calignano et al. 2015; Zwaan et al. 2016). Other substances, such as paraffin and gelatin mixtures can be applied when power-law or temperature-dependent rheological behaviour is required (e.g. Zulauf & Zulauf 2004; Boutelier & Oncken 2011). In lithosphere-scale models, the weak ductile behaviour of the asthenospheric mantle is simulated with low viscosity materials, such as honey, glucose syrup or even pure water (Mart & Dauteuil 2000; Chemenda et al. 2002; Schellart et al. 2002; 2003; Molnar et al. 2017). These normally exhibit Newtonian behaviour. Further details and references concerning the above-mentioned and other analogue model materials can be found in a comprehensive review article by Schellart & Strak (2016).

### 1.3 This study

The analogue modelling work summarized above reveals a trend from a rather qualitative modelling approach to a more quantitative approach. Older studies tend to present a range of models with widely different parameters (for materials and set-up), which are often not fully described. By contrast, newer studies often specify such data in much detail, allowing repetition by analogue and also numerical means. Yet direct comparisons between the various methods remains challenging, especially since these methods aim to simulate different tectonic settings (see also sections 2.2 and 2.3). In theory, the scaling principles that have elevated analogue modelling from a qualitative to a quantitative method can be applied to compute how models should compare to each other (e.g. Hubbert 1937; Ramberg 1981; Weijermars & Schmeling 1986). In practice, however, such calculations remain approximate. Different material handling techniques (laboratory traditions, the human factor) or climatic conditions (room temperature, humidity) may influence material behaviour and thus model results with the same set-up can vary from laboratory to laboratory (e.g. Krantz 1991; Schreurs et al. 2006, 2016; Rudolf et al. 2015). Furthermore, our understanding of experimental material rheology may be incomplete or poorly constrained since some parameters are difficult to properly determine (Eisenstadt &

173  Sims 2005; Dooley & Schreurs 2012). Thus the need for reference studies of lithospheric
174  extension with standardized model parameters remains and to our knowledge no such work is
175  available to date.
176
177  The aim of this study is to systematically compare a series of simple crustal-scale, normal-
178  gravity laboratory experiments involving commonly used set-ups and to discuss the tectonic
179  settings to which these would apply. We use either a foam base, a rubber base, rigid base
180  plates or "conveyor belt" style plastic sheets as a mechanism to deform the overlying brittle or
181  brittle-viscous model materials. This forms a total of 8 reference set-ups. Various additional
182  sub-set-ups serve to examine, among others, the effects of varying extension velocity, layer
183  thickness and brittle-to-viscous thickness ratio. We also apply X-ray computed tomography
184  (XRCT or CT) for obtaining a highly detailed 3D view of internal as well as external model
185  evolution.
186
187
188  **2. Materials and methods**
189
190  2.1 Material properties
191
192  We ran brittle (single-layer) and brittle-viscous (two-layer) experiments to simulate a brittle
193  upper crust and a complete brittle-ductile crust, respectively (Fig. 2). Reference brittle-only
194  experiments contain a 4 cm thick layer of fine quartz sand (ø = 60-250 $\mu$m). The sand is sieved
195  from ca. 30 cm height into the experimental apparatus to guarantee a sand density of ca. 1560
196  kg/m$^3$ . The sand is flattened using a scraper at every cm thickness during preparation of the
197  experiment, causing slight density variations, which subsequently appears on CT images as a
198  "layering" (Fig. 2f, g). The reference experiments with a brittle-ductile set-up are built of an
199  additional 4 cm thick, near-Newtonian viscous layer (viscosity $\eta$ = ca. 1.5·10$^5$ Pa·s; stress
200  exponent n = 1.05) consisting of a 1:1 weight mixture of SGM-36 Polydimethylsiloxane (PDMS)
201  silicone and corundum sand ( $\rho_{specific}$ = 3950 kg/m$^3$, Panien et al. 2006; Zwaan et al. 2016;
202  Carlo AG 2018). The obtained density of the viscous material (ca. 1600 kg/m$^3$) is close to that
203  of the overlying quartz sand layer (1560 kg/m$^3$). This results in a density profile that avoids
204  buoyant rise of the viscous material that would occur for pure, low density PDMS ( $\rho$ = 960
205  kg/m$^3$). Further material properties are listed in Table 1.
206
207  2.2. Experimental design
208
209  The experimental apparatus consist of a fixed base and two longitudinal sidewalls, which can
210  move outward independently from each other above a fixed support table, controlled by precise
211  computer-guided stepper motors. The initial width of the experiment is 30 cm in all set-ups,
212  which is considerably less than the model length (as specified below). This high length-to-width
213  ratio diminishes the influence of boundary effects of the short sidewalls. Through modification
214  of the apparatus we can use four different methods to transfer deformation from the base of the
215  set-up to the overlying experimental materials: by applying either a foam base or rubber sheet
216  base for a distributed deformation setting, or a base of rigid plates or conveyor belt system for
217  focussed deformation (Fig. 2). The confinement along the short sidewalls varies according to
218  the set-up, as explained below. Since the various set-ups differ significantly, we also specify
219  which type of tectonic setting or crustal rheology is simulated (Fig. 3). An additional overview of
220  the similarities and differences between our set-ups by means of (relative) velocities and shifts
221  in reference frames is provided in Appendix A (Fig. A1).
222
223  2.2.1. Distributed deformation set-ups
224
225  A foam base (F series experiments) induces distributed deformation (e.g. Schreurs & Colletta
226  1998; Schlagenhauf et al. 2008; Zwaan et al. 2016, Zwaan & Schreurs 2017). An 8 cm thick
227  RG 50 Polyurethane foam base is first compressed between the sidewalls with the model
228  subsequently constructed on top (Fig. 2a-c). As the sidewalls move apart during an experiment,
229  the foam expands, causing deformation in the overlying materials (Fig. 2b, c). Rubber sidewalls

230  at the short ends of the set-up confine the materials, with the distributed extension of the rubber
231  decreasing boundary effects there (Fig. 2a). All foam base experiments have a length of 79 cm
232  for an initial length-to-width ratio of 2.6.

234  For the rubber base set-up (R series experiments) a 1.5 mm thick Neoprene rubber sheet is
235  spanned between the two long sidewalls (e.g. Vendeville et al. 1987; Bahroudi et al. 2003;
236  Bellahsen et al. 2003; Bellahsen & Daniel 2005; Fig. 2d-f). Note that this is slightly different
237  from set-ups applying a rubber sheet between two rigid base plates that are subsequently
238  moved apart (e.g. McClay & White 1995, McClay et al. 2002; Corti et al. 2007; Henza et al.
239  2010). We use a full rubber base for our experiments in order to allow a comparison with the
240  foam base set-up. When the long sidewalls move apart, the rubber sheet is stretched and
241  extends uniformly with a constant velocity gradient, causing distributed deformation (Fig. 2e, f).
242  The sides of the set-up are free, that is, not confined by any sidewall that may influence the
243  experiments, for the experiments with only a brittle layer. The short sidewalls of the brittle-
244  ductile rubber base experiments are enclosed by a sand talus so that the viscous material
245  cannot escape sideways (Fig. 2d). Since the large forces involved in stretching a large rubber
246  sheet may cause damage to the experimental apparatus, the length of the rubber base
247  experiments is kept to 50 cm. Therefore, the initial length-to-width ratio is 1.7.

249  Previous authors have applied a rubber or foam base with an overlying brittle layer to model
250  distributed thin-skinned extension (e.g. Bahroudi et al. 2003; Schlagenhauf et al. 2008). In
251  nature, distributed extension in the brittle crust could develop in a setting with high brittle-ductile
252  coupling between a brittle upper crust and a strong ductile lower crust (Fig. 3a), either due to
253  high strain rates or high viscosity (Brun 1999, Buiter et al. 2008; Zwaan et al. 2016). Note that
254  the sub-crustal mantle has no influence in this case. By contrast, a set-up with brittle-viscous
255  layers on top of a rubber or foam base would simulate a normal brittle-ductile crust on top of a
256  viscously deforming weak mantle (Fig. 3b). This setting, in which the strength of the lithosphere
257  is determined by the brittle crust (Bürgman & Dresen 2008), can be expected in a hot
258  lithosphere, for instance above a mantle plume (Saunders et al. 1992; Burov et al. 2007) or
259  after a phase of crustal thickening and radiogenic heating (Brun 1999).

261  2.2.2. Localized deformation set-ups

263  The plate base set-up (P series experiments) involves two 3 mm thick rigid plastic plates that
264  are fixed to the long sidewalls (Fig. 2g-h) (e.g. Allemand & Brun 1991; Tron & Brun 1991; Brun
265  & Tron 1993; Bonini et al. 1997; Keep & McClay 1997; Michon & Merle 2000). When these
266  plates move apart with the long sidewalls, velocity discontinuities (VD) develop at the basal
267  edges of the plates. The support table below the plates prevents material from escaping (Fig.
268  2e, f). The short sidewalls are confined by a similar plate system that is fixed to the horizontal
269  plates, thus moving in sync and creating the same boundary conditions as at the base of the
270  apparatus (Fig. 2g). In contrast to the set-ups applying distributed extension described above,
271  the rigid base plates allow both symmetric and asymmetric extension (Fig. 2e, f). In the former
272  case, two moving VD's occur as the edges of both non-overlapping plates move apart, whereas
273  the latter case results in only one VD (similar to Michon & Merle 2000, see also Fig. A1). The
274  initial length of the base plate experiments is 90 cm, so that the length-to-width ratio is 3.
275  Although we did not measure the boundary friction of the plastic plates with quartz sand, it is
276  likely to be close to the values reported by Panien et al. 2006 for plastic and PVC: ca. 20.7˚.

278  The final set-up is a modified version of the plate base set-up involving a "conveyor belt" type of
279  deformation (C series experiments) (e.g. Allemand & Brun 1991; Tron & Brun 1991; Dauteuil &
280  Brun 1993; Keep and McClay 1997; Román-Berdiel et al. 2000). Sub-mm thick plastic sheets
281  or foil ("Alkor" foil 120010 formerly produced by Alkor-Venilia and now available as "Gekkofix
282  11325" www.gekkofix.com; Klinkmüller et al. 2016) are fixed to the plate base set-up and are
283  led down through a slit in the support table, along the central axis of the experiment (Fig. 2j-l).
284  When the long sidewalls move apart, the sheets are pulled upward through the slit (Fig. 2k, l).
285  In contrast to the plate base experiments, a single VD occurs, which remains located at the
286  centre of the experiment. Since this is true for both symmetrical and asymmetrical experiments

287 (Fig. 2k, l), the two setups are different. But the asymmetric set-up is, after a switch of
288 reference frame, the same as the asymmetric plate base set-up (Fig. A1) and should thus
289 produce an identical result. The same sheet system is applied on the short sidewalls in order to
290 have a continuous confinement (Fig. 2j). These sheet base experiments have the same length-
291 to-width ratio as the base plate experiments, i.e. 3. The angle of boundary friction of the foil
292 with quartz sand lies between 15˚ and 21˚ (Schreurs et al. 2016).

294 Both the base plate and conveyor base experimental designs involve localized deformation at
295 VDs. These VDs simulate a fault in a strong layer underlying the experimental materials. In the
296 case of our brittle-only experiments, this would translate to a fault at the base of the upper crust.
297 In order to have a fault in the lower crust, the latter needs to behave in a brittle fashion, which
298 in our case would be expected in an old, cool crust (Fig. 3c). On a smaller scale, one can also
299 interpret the VD as a reactivated basement fault affecting overlying strata (e.g. Acocella et al.
300 1999; Ustaszewski et al. 2005). Concerning our brittle-viscous crustal set-up, the VD translates
301 to a fault in a strong upper mantle (e.g. Allemand & Brun 1991; Michon & Merle 2000). Such a
302 setting can be expected in a young stable lithosphere with a strong brittle mantle (Fig. 3d).

304 2.3. Additional experimental parameters

306 For every experimental set-up, we test brittle-only materials and brittle-viscous layering, with a
307 reference layer thickness of 4 cm, so that brittle-only and brittle-viscous experiments are 4 cm
308 and 8 cm thick, respectively. However, for specific experiments, we either apply a 4 cm thick
309 brittle-viscous layering, or we modify the brittle-to-viscous thickness ratio by decreasing the
310 thickness of the viscous layer to 2 or 1 cm, in order to capture the effects that a different crustal
311 layering may have on extensional structures (details in Table 2). This decrease in viscous layer
312 thickness can be either due to a thinner, viscous lower crust, assuming that the brittle crustal
313 thickness remains the same (Fig. 3g, h), or an increase in brittle crustal thickness with a
314 constant Moho depth. In both cases, this would result in a relative strengthening of the
315 lithosphere with respect to the default layering.

317 We also apply "seeds" to localize deformation in several experiments (Fig. 2, Table 2). These
318 seeds are 1 cm thick, semi-cylindrical viscous rods of the previously described
319 PDMS/corundum sand mixture that are placed at the base of the brittle layer. The seeds are
320 continuous and stretch along the full axis of the experiment. They form weak zones where
321 deformation may localise, since the strong sand cover is locally thinner and thus weaker (e.g.
322 Zwaan et al. 2016). Although we acknowledge that surface processes can influence rift
323 evolution (e.g. Burov & Cloetingh 1997; Bialas & Buck 2009; Zwaan et al. 2017), we neither
324 apply erosion nor sedimentation in our experiments, since we aim to directly evaluate
325 differences in experimental results obtained by differences in simple experimental set-ups.

327 Our reference extension velocity is 8 mm/h, with both long sidewalls moving 4 mm/h for
328 symmetrical extension, or a single sidewall moving 8 mm/h for asymmetrical extension (Fig. 2).
329 Considering a reference duration of 5 h, the total extension equals 40 mm (or ca. 13%, given
330 an initial width of ca. 30 cm). In addition, we varied extension velocity for selected experiments.
331 In the case of the brittle-only experiments, this should not affect the brittle deformation
332 structures because of the time-independent behaviour of sand. For brittle-viscous experiments
333 however, variations in extension velocity are equivalent to variations in effective linear viscosity
334 and will thus affect the relative strength contrast between the brittle and viscous materials (Fig.
335 3e, f). In the experiments with a foam or rubber base, a strengthening of the viscous material,
336 due to an increase in extension velocity, translates to a strengthening of the hot lithosphere
337 with increased brittle-ductile coupling but still a relatively weak mantle (compare Fig. 3b with
338 Fig. 3e). In the base plates or conveyor set-up equivalent, a higher extension velocity would
339 would then represent a normal crust with increased coupling with respect to the reference
340 settings (Fig. 3f).

342 A thin (ca. 0.5 mm thick) grid made of dark (corundum) sand with a 4 x 4 spacing applied to the
343 surface of each experiment allows a first-order assessment of surface deformation by means of

344 top view images, without influencing the experimental results. Furthermore, every component
345 of the machine around the experiment consists of X-ray transparent materials to allow for CT-
346 scanning and various experiments are analysed with CT-techniques to reveal their 3D internal
347 evolution (Fig. 2b). Most experiments marked in Table 2 as "CT-scanned" were a rerun of
348 previous tests performed without CT scanning. Various other experiments were also repeated
349 and did indicate little structural variation, thus good reproducibility is ensured (Table 2, details
350 presented in Appendix B, Figs. B1, B2).
351
352
353 2.4. Scaling
354
355 We calculate stress ratios ($\sigma^* = \sigma_{experiment}/\sigma_{nature}$) using (Hubbert 1937; Ramberg 1981): $\sigma^* =$
356 $\rho^* \cdot h^* \cdot g^*$ where $\rho^*$, h* and g* represent the density, length and gravity ratios respectively.
357 The strain rate ratio $\dot{\varepsilon}^* =$ is derived from the stress ratio σ* and the viscosity ratio η*
358 (Weijermars & Schmeling 1986): $\dot{\varepsilon}^* = \sigma^*/\eta^*$. The velocity ratio v* and time ratio t* can be
359 obtained as follows: $\dot{\varepsilon}^* = v^*/h^* = 1/t^*$. Natural values for lower crustal viscosity may have a wide
360 range depending on the specific tectonic setting (η = $10^{19}$-$10^{23}$ Pa·s, e.g. Buck 1991; Brun
361 1999; Bürgman & Dresen 2008). We assume an intermediate lower crustal viscosity of $10^{21}$
362 Pa·s, which is in line with recent findings (Shinevar et al. 2015, and references therein). An
363 hour in our experiments thus translates to 0.84 Ma in nature and our reference velocity (8
364 mm/h) converts to a velocity of ca. 0.5 mm/y in nature, close to typical values for initial
365 continental rifting (1-5 mm/y, e.g. Saria et al. 2014). The scaling parameters are summarized in
366 Table 3.
367
368 To ensure dynamic similarity between brittle natural and experimental materials, we calculate
369 the ratio $R_s$, which is a function of gravitational stress and cohesive strength (C) (Ramberg
370 1981; Mulugeta 1998): $R_s = (\rho \cdot g \cdot h)/C$. When adapting an intermediate cohesion of ca. 8
371 MPa for upper crustal rocks, we obtain a $R_s$ value of 67 for both nature and our experiments.
372 This cohesion is relatively low compared to the ca. 20-40 MPa measured for continental rocks
373 (e.g. Handin 1969; Jaeger & Cook 1976; Twiss & Moores 1992), but should be reasonable
374 given that the strength of the earth's crust is generally reduced due to previous phases of
375 tectonic activity. For viscous materials, the Ramberg number $R_m$ applies (Weijermars &
376 Schmeling 1986): $R_m$ = gravitational stress/viscous strength = $(\rho \cdot g \cdot h^2)/(\eta \cdot v)$. Our
377 experimental and the equivalent natural $R_m$ values are the same at 75.
378
379
380 **3. Results**
381
382 3.1. Foam base experiments (F series)
383
384 Fig. 4 shows the results of two brittle-only foam base experiments. Experiment F1 (without
385 seed) develops no distinct features except for significant boundary effects along the
386 longitudinal sidewalls towards the end of the experiment (Fig. 4a). In contrast, the seed in
387 experiment F4 localizes deformation in the centre of the experiment, although faulting along the
388 long sidewalls is also visible at the surface (Fig. 4b). The CT data from experiment F4 (with
389 seed) reveals the evolution of these structures in more detail (Fig. 4c-e). After ca. 60 min (8
390 mm) of extension, a graben starts forming above the seed and becomes visible at the surface
391 after 120 min (16 mm of extension, Fig. 4d, f). This main rift structure continues developing
392 towards the end of the experiment (Figs. 4e, g). The CT images show how additional faulting
393 occurs: first along the sidewalls (Fig. 4d, f), later on throughout the experiment so that at the
394 end of the experiment, pervasive sidewall-parallel striking normal faulting is omnipresent (Fig.
395 4e, g). Note that this distributed faulting is not visible on the top view images due to the low
396 fault offsets at the surface that do not cast shadows on the model surface (Fig. 4b), and may
397 very well be present in the experiment without seed as well (F1, Fig. 4a). In Experiment F4, the
398 brighter tones at the rift shoulders visualise local uplift: parts of the experiment that are uplifted
399 present less of a barrier to the X-rays since these pass through less material, which shows up

400 as a brighter colour on CT images. It is however important to stress that these brighter colours
401 do not represent a specific altitude.
402
403 The evolution of foam base experiments with a brittle-viscous layering is summarized in Fig. 5.
404 Experiment F5, without a seed, forms no central graben (Fig. 5a). Instead, all deformation is
405 concentrated as boundary effects along the long sidewalls. By contrast, experiment F7, with a
406 seed, produces a well-developed symmetric graben structure. Still also this set-up produces
407 some minor faulting along the long sidewalls (Fig. 5b). CT images illustrate the 3D evolution of
408 experiment F7 (Fig 3c-g). Soon after initiation (30 min, 4 mm extension), a central graben
409 structure with two main boundary faults develops above the seed. As the experiment
410 progresses, this structure continues evolving: the rift basin grows deeper and the brittle
411 material situated between the initial boundary faults starts breaking up due to internal faulting
412 (Fig. 5d, f). Some boundary effects develop, but are relatively minor with respect to the central
413 graben structure (Fig. 5d-g). Towards the end of the experiment the brittle sand is almost
414 breached by the upwelling viscous layer (Fig. 5e g). In this experiment, deformation is strongly
415 focussed on the rift structure and no distributed faulting can be distinguished. As in the brittle-
416 only set-up with a seed (F4), this experiment also develops rift shoulder uplift, as indicated by
417 the bright colours at the model surface (Fig. 5e).
418
419
420 3.2. Rubber base experiments (R series)
421
422 The surface evolution of two selected rubber base experiments built of only sand is depicted in
423 Fig. 6. Experiment R1 (Fig. 6a, a') has no seed to localize deformation and, as a consequence,
424 deformation focuses along the sidewalls. In addition, remarkable conjugate faults develop at
425 the end of the experiment (300 min, 40 mm of extension), but are not well visible on the top
426 view images due to poor lighting conditions (Fig. 6a). However, an additional phase of
427 extension (30 min at 40 mm/h) helps to highlight these conjugate faults (Fig. 6a'). In contrast to
428 experiment R1, experiment R5 contains a viscous seed that focuses faulting along the central
429 axis of the experiment (Fig. 6b). As a result, this experiment develops a central graben
430 structure. Similar to experiment R1, well-defined conjugate faults occur as well.
431
432 The CT-derived 3D images (Fig. 6c-g) reveal how deformation localizes along the seed and the
433 sidewall in the initial stages of experiment R5, forming a cylindrical rift structure (Fig. 6d).
434 However, after some 20-25 mm of extension, conjugate sets of vertical strike-slip faults start
435 developing (Figs. 6f), which become pervasive toward the end of the experiment (Figs. 6e, g).
436 This curious feature is the result of along-strike compression, as the orthogonally extending
437 rubber sheet contracts perpendicular to the extension direction (Fig. 6a'). Yet the graben
438 structures continue to evolve toward the end of the experiment run (Fig. 6e, g). The brighter
439 colours on the surface seen in Fig. 6g again indicate rift shoulder uplift.
440
441 Fig. 7 shows results of four brittle-viscous rubber base experiments. Experiment R7, without
442 seed, produces no clear surface structures except for the strong boundary effects along the
443 sidewalls (Fig. 7a). In contrast, experiment R8, with seed, experiences early fault localization
444 (after 30 min a rift becomes visible at the surface), which continues evolving towards the end of
445 the experiment (Fig. 7b). However, also this experiment develops strong boundary effects
446 along the long sidewalls and at the corners, where some viscous material flows into the gap
447 between the original sand buffer and the retreating sidewalls. The rift structure is best
448 developed in the centre of the experiment and dies out towards the short sidewalls, involving
449 slight block rotation of the sand layer in the four corners of the experiment (Fig. 7b).
450
451 Experiment R9 at an increased extension velocity of 80 mm/h (Fig. 7c) produces a central rift
452 that is quite similar to the rift in experiment R8 (Fig. 7b), even though no seed is included.
453 Significantly higher extension velocities (480 mm/h in experiment R10) result in strongly
454 distributed deformation with multiple rifts (Fig 5d). The three experiments without a seed at
455 different extension rates (Fig. 7a, c, d) examine the effect of decreased strength contrast
456 between the brittle and viscous layers. We will discuss this further in discussion section 4.4.

3.3. Plate base experiments (P series)

Experiments P1 and P2 consist of a brittle sand layer on top of plastic-covered rigid base plate(s) (Figs. 1g, 8a, b). In experiment P1 we apply symmetric extension, whereas in experiment P2 extension is asymmetric. Both experiments initially develop a rift above the velocity discontinuity along the central axis of the experiment. However, with continued extension experiment P1 develops a graben with a central horst block in the middle, which does not develop in experiment P2 (Fig. 8a, b). Otherwise, both grabens have the same width. No boundary effects occur along the long sidewalls.

Fig. 8c-g shows the results of the brittle-viscous base plate experiments. Experiments P3 and P7 are following symmetrical and asymmetrical extension, respectively. No seed is included. The structural evolution is similar for both experiments. Rifting initiates at the short sidewalls, where both the base plates and confining plates are moving apart (Figs. 1h, 8c, d). These rifts propagate slightly towards the centre of the experiment, but strong boundary effects along the long sidewalls take up much of the extension there and no continuous rift structure develops in the centre of the experiment (Fig. 8c, d). As a result, block rotation takes place on both sides of the propagating rifts. The surface structures are largely the same in both experiments, suggesting that the application of symmetric or asymmetric extension does not have a significant influence in this set-up.

The application of a seed on top of the viscous layer (Exp. P10, in symmetric extension) results in early localization and rift development along the central axis of the experiment (Fig. 8e). This structure continues developing throughout the experiment, yet more extension is accommodated towards the short sidewalls than the middle section, where boundary effects along the long sidewalls take up a larger part of the deformation, similar to experiments P3 and P7 (Fig. 8c, d).

The thick viscous layer in experiments P3 and P7 likely dampens the influence of the basal boundary condition on the sand layer. We therefore run further tests with half the layer thickness for the viscous material, keeping the same brittle-to-viscous ratio (2 cm brittle and 2 cm viscous material, without seed). These experiments did not produce a continuous graben structure either. However, experiment P9, with a higher 80 mm/h extension velocity (and again 2 cm brittle and 2 cm viscous layers, without seed), produces interesting basin geometries (Fig. 8f, g). Instead of developing a simple rift structure, the viscous layer at the centre of the experiment is strongly stretched, creating a depression with continuous rift basins at its margin due to what seems to be passive downbending (Fig. 8g). Secondary graben structures develop further away from the central depression, indicating a degree of distributed deformation. Notably, no boundary effects occur along the long sidewalls, in contrast to the other brittle-viscous plate base experiments.

3.4. Conveyor base experiments (C series)

Fig. 9 shows the results of the conveyor base set-up with only a brittle layer (experiments C1 and C3). Both experiments develop a large rift structure along the central axis of the experiment (Fig 9a, b), rather similar to the plate base experiments P1 and P2 (Fig 8a, b). We do, however, not observe a difference between the symmetrical and asymmetrical set-ups.

The results of the brittle-viscous experiments show more diversity than their brittle-only counterparts (Fig. 9c-g). Experiment C4, with symmetrical extension, develops two rifts that originate from the short sidewalls and propagate towards the experiment centre (Fig. 9c). They do however not connect, as boundary effects along the long sidewalls take up most of the deformation in the centre, similar to the structures observed in the plate base equivalents (experiments P3 and P7, Fig. 8c, d). We did not run an asymmetrical extension experiment. Instead, we attempted to reduce the boundary effects along the short sidewalls by applying lubricants or adding a sand buffer as proposed by Tron & Brun (1991) (experiments C5 and C6,

514  respectively). Unfortunately, the boundary effects remained or got worse (See Appendix B, Fig.
515  B1). Furthermore we ran the conveyor base equivalent of experiment P9 (2 cm sand, 2 cm
516  viscous material, Fig. 8f, g), labelled C12, with very similar results to experiment P9 (Fig. B2).
517
518  We also tested the effect of decreasing viscous layer thickness, thus increasing the brittle-to-
519  viscous ratio, in experiments C7 and C8. In experiment C7 (Fig. 9d), the thickness ratio is 2,
520  which does not lead to a significantly different structural evolution compared to the reference
521  setup of experiment C4 (Fig. 9c). However, decreasing the viscous layer thickness further to 1
522  cm (ratio: 4), leads to localization of faulting along the central axis of the experiment during
523  early stages of the experiment, whereas rifting becomes more widespread towards the end of
524  the experiment (C8, Fig. 9e). Tests with higher extension velocities (80 and 40 mm/h for
525  experiments C9 and C10/C11, respectively, see Table 2 and Appendix B, Fig. B2) have shown
526  to improve rift localization, and one such experiment was run in a CT scanner (experiment C11,
527  Fig. 9f, g). These experiments all develop the same features: a double rift system on either side
528  of the VD, which internally grows more complex with time. We also observe the development of
529  further, minor additional rift basins striking parallel. Slight boundary effects occur along the long
530  sidewalls in experiments C10/C11 as well (Fig. 9f, g).
531
532
533
534  **4. Discussion**
535
536
537  4.1. General structures
538
539  We present a schematic overview of our experimental results in Fig. 10, summarizing the
540  general structures in map view and section, and Table 4, linking these observation with
541  potential natural settings. A clear distinction exists between the brittle-only experiments (left-
542  hand half of upper three rows in Fig. 10) and the brittle-viscous experiments (right-hand half of
543  upper three rows in Fig. 10) since the viscous layer acts as a buffer between the deformation-
544  inducing base and the overlying sand. In the brittle-only experiments, no such buffer exists and
545  deformation induced by the model base is directly transmitted to the overlying sand cover,
546  leading to more distinct structural differences between the experimental series. In addition, the
547  bottom row of Fig. 10 summarizes the structures observed in the high extension velocity
548  experiments and the tests with high brittle-to-viscous ratios. Our experimental results are
549  discussed in more detail below.
550
551  4.2. Brittle-only experiments
552
553  In the foam base experiments, the sand above the foam directly experiences the distributed
554  deformation induced by the expanding foam, causing fault development throughout the
555  experiment, but mainly along the long sidewalls (Figs. 4a, 10a). Schlagenhauf et al. (2008)
556  report similar but more pronounced distributed rifting, possibly enhanced by a higher degree of
557  extension of their foam base (20% vs. our 13%) and a thicker sand pack (8 cm vs our 4 cm).
558  Seeds do localize rift basins in our experiments, but these structures only account for a minor
559  part of the extension as the rifts experience little subsidence with respect to most other
560  experiments (e.g. P1 and P2 in Figs. 8a, b). The brittle-only rubber base experiments produce
561  similar structures to the brittle-only foam base experiments: distributed deformation and a minor
562  axial rift when a seed is applied (Fig. 6). Significant faulting develops at the long sidewalls and
563  migrates towards the centre of the experiment (Fig. 6c-g), which could be explained by stronger
564  strain gradients in the rubber near the sidewalls (Ackermann 1997). A similar effect could
565  possibly occur in the foam base experiments as well, explaining the comparable boundary
566  effects.
567
568  The rubber base experiments also develop conjugate strike-slip faults due to the contraction of
569  the rubber perpendicular to the extension direction (Poisson effect) (Smith & Durney 1992;
570  Venkat-Ramani & Tikoff 2002). Such structures are not always observed in other model studies

571 applying a rubber base set-up (e.g. Vendeville et al. 1987, Fig. 11a). The Poisson effect-related
572 structures we obtain are probably due to the relatively low length-to-width ratio rubber base we
573 use (ca. 1.7). Rubber base models by McClay & White (1995) and McClay et al. (2002) with
574 much higher length-to-width ratios (6 and 4, respectively) do not undergo any visible
575 contraction perpendicular to the extension direction, whereas an experiment by Bahroudi et al.
576 (2003) with a length-to-width ratio of 0.8 develops strong conjugate faulting (Fig. 11b). The
577 faults in Bahroudi et al. (2003) have a normal fault component as well, possibly because the
578 rubber was stretched from one side only. It is furthermore interesting to note that the Poisson
579 effect may occur in very different types of models or materials. Chemenda et al. (2002) for
580 instance, applying an elasto-plastic mixture of various components floating on water to simulate
581 the lithosphere and asthenosphere, also obtain pervasive conjugate faults due to extension-
582 perpendicular contraction.
583
584 Contrary to their rubber and foam base equivalents, a strong localization of faulting above the
585 velocity discontinuity (VD) occurs in the brittle-only plate base and conveyor base experiments
586 (Figs. 8a, b, 9a, b, 10i, j). The plates and sheets translate overlying materials, except at the
587 velocity discontinuity, where extension localises and deep rift basins form. The centre of the rift
588 basins in both the asymmetric and symmetric experiments lies practically at the same level as
589 the experimental base at the end of the experiment (4 cm depth, scaling to a 20 km deep basin
590 in nature, Fig 8i, j). In nature, isostatic compensation would have reduced basin depth. These
591 set-ups may therefore perhaps best be used for investigating initial (small) amounts of
592 extension (e.g. maximum half the thickness of the brittle crust), or larger amounts of extension
593 when significant sedimentation is applied (e.g. Allemand & Brun 1991; Brun & Tron 1993; Keep
594 & McClay 1997). The small horst structure along the axis of the symmetric extension plate base
595 experiment (Figs. 8a, 10i) is likely formed when both plates move away, leaving a small
596 quantity of material behind in the middle. Previous authors have shown the impact extension
597 asymmetry can have on rift geometry by creating strongly asymmetric graben structures
598 (Allemand et al. 1989; Allemand & Brun 1991; Panien et al. 2005, Fig. 11c, d). Yet these effects
599 are not directly observed in our experiments, possibly due to the relatively minor total extension,
600 the lack of syn-rift sedimentation or because we lack the necessary cross-sections as these
601 models were not CT-scanned.
602
603 4.3. Brittle-viscous experiments
604
605 The presence of a viscous layer in our experiments leads to quite different structures with
606 respect to those observed in their brittle-only counterparts (Fig. 10). The brittle-viscous foam
607 and rubber base cases produce basically the same structures: when no seed is present,
608 faulting occurs only along the sidewalls, whereas a seed concentrates deformation, resulting in
609 a central rift structure (Figs. 5a, b, 7a, b, 10c, d, g, h). The decoupling from the foam or rubber
610 base allows the brittle cover to behave as rigid blocks, more or less passively floating on the
611 viscous layer (Zwaan et al. 2017), whereas the sand in the brittle-only experiments is directly
612 coupled to the base, forcing a pervasive type of faulting (Fig. 10a, b, e, f). Due to this
613 decoupling effect of the viscous layer, no conjugate strike-slip fault sets occur in the brittle-
614 viscous rubber base experiments, similar to the experiments of Bellahsen et al. (2003). The fact
615 that the rifts in our rubber base experiments are less developed towards the short ends of the
616 set-up is most likely caused by the use of a sand talus to contain the viscous material there
617 (Figs. 2d, 6, 7b-d). This creates a deformation contrast between the immobile talus and the
618 deforming material above the rubber sheet, an effect that could potentially be reduced by using
619 a rubber sidewall, as in the foam set-up (Fig. 1a).
620
621 In contrast to the brittle-only experiments, the results of the brittle-viscous plate base and
622 conveyor base experiments are quite similar to their foam and rubber base equivalents (Fig.
623 10), most likely due to the tendency of the viscous material to easily spread out when subject to
624 extension. All of these experiments, however, see minor rifting initiating at the short sides of the
625 set-up, because there the model is confined by sidewalls or sheets that move in sync with the
626 long sidewalls, imposing the same boundary conditions there as at the base of the set-up. The
627 resulting additional drag enhances the extensional deformation at these short edges, forcing

628 the development of rifts, which propagate toward the centre of the experiment (Figs. 8c-e, 9c, d,
629 10k). In the centre, however, the viscous spreading mechanism is dominant, so that we
630 observe the same structures as in the other brittle-viscous experiments (Fig. 10). This "short
631 sidewall effect", which is also present when applying a seed, causing the rifts to be more
632 developed at the short ends of the experiment (Figs. 8e, 10l), may also have occurred in a
633 model by Mart & Dauteuil (2000). Their experiment involves a curious propagating rift system,
634 initiating at the short edge of the set-up, which has a similar plate confinement as in our
635 experiments. In order to reduce this type of boundary effects, higher strain rates can be applied
636 (Fig. 9). The use of a sand talus to confine the short ends of the experiment as suggested by
637 Tron & Brun (1991) does not reduce these boundary effects in our experiments, as the sand
638 has an even stronger rigid relation to the experimental materials as the side plates (or sheets)
639 (experiment C5, Appendix B2).

641 As with the reference brittle-only experiments, we do not observe a clear difference between
642 symmetric and asymmetric extension on the scale of our set-ups. Yet previous authors have
643 shown that asymmetric extension may have an effect in brittle-viscous settings as well. This is
644 however mostly in combination with a relatively thin viscous layer that enhances brittle-viscous
645 coupling (e.g., Allemand et al. 1989). By contrast the relatively thick viscous layer in our
646 reference models acts as a buffer, decoupling the sand from the asymmetrically extending
647 plates or sheets (see also section 4.5).

651 4.4. Velocity effects: wide rifting versus passive downbending and marginal basin formation

653 As discussed in section 4.2, the brittle-viscous foam and rubber base experiments without a
654 seed lack the brittle-viscous coupling necessary to transfer deformation to the brittle layer.
655 Stronger coupling can be achieved by either using a material with a higher viscosity or by
656 increasing the extension velocity (which effectively increases viscosity) as in experiments R9
657 and R10 (Fig. 7c, d). A higher viscosity would allow the transfer of distributed extension applied
658 by the base to the brittle layer and thus lead to distributed or wide rifting (Brun 1999; Buiter et al.
659 2008; Zwaan et al. 2016; Figs. 7c, d, 10m, m'). Note that the central rift in experiment R9 is not
660 localized by a seed (Fig. 7c), but probably forms due to some wide rifting effect: the higher the
661 extension velocity (while keeping all other parameters constant), the higher the brittle-viscous
662 coupling and the more rifts develop, as illustrated by experiment R10 (Fig. 7d). Still the type of
663 deformation in these experiments is not as evenly distributed as in their brittle-only equivalents
664 (Figs. 4, 10a, a', b, b', e, e', f, f'), probably since brittle-viscous coupling is not high enough.

666 Considering the results from the high velocity rubber base experiments R9 and R10 (Fig. 7c, d,
667 10m, m'), those of the high velocity brittle-viscous plate/conveyor base experiments P9 (Fig. 8f)
668 and C12 (Fig. B2) may seem somewhat remarkable; instead of developing distributed rifting,
669 these models generate a 'down-bent' depression bordered by marginal grabens (Figs. 8f, g,
670 10n, n', B2). It seems that the high extension velocity in P9 and C12 (80 mm/h, translating to
671 320 mm/h for the reference layer thickness) causes high coupling between the viscous layer
672 and the brittle cover, as well as between the viscous layer and the base. The set-ups lead to
673 intense stretching (necking) above the VD(s) and subsequent downward 'bending' of the sand
674 cover (Fig. 8g). High coupling between the viscous layer and the base also explains why no
675 apparent boundary effects are visible along the longitudinal sidewalls. The bending of the brittle
676 layer at the edge of the system causes local extension in the sand and the formation of
677 marginal basins. Similar structures can be observed along the Western Escarpment of the Afar
678 (northernmost sector of the East African Rift System) in Ethiopia (e.g. Abbate & Sagri 1969;
679 Chorowicz et al. 1999), possibly caused by loading and bending due to massive diking and
680 underplating in the adjacent rift basin (Corti et al. 2015). Our experiment may suggest that rapid
681 extension of the crust could also cause such basin geometries.

4.5. Effects of different brittle-to-viscous ratios

Our brittle-viscous plate and conveyor base set-ups with the reference brittle-to-viscous thickness ratio fail to produce proper rift basins, in contrast to their brittle-only equivalents (experiments P1, P2, C1 and C2, Figs. 8a-d, 9a,b, 10k). Instead, we either need a seed as in the foam and rubber base experiments (experiment P10, Figs. 8e, 10l), or a high brittle-to-viscous thickness ratio (>2) to localize deformation (experiments C8 and C11, Fig. 9e-g). In the latter case, high extension velocities improve localization (experiment C11, Fig. 9f, g). Yet we obtain double rift structures rather than the single rift basins in the brittle-only experiments.

Also Tron & Brun (1991) apply a relatively thin viscous layer (brittle-to-viscous ratio of ca. 2) and obtain well-developed rift structures in symmetric extension (Fig. 11f). The thin viscous layer probably increases brittle-viscous coupling, causing the experimental brittle materials to behave as rigid blocks and leading to rift localization near the VD, similar to our brittle-only experiments (Fig. 8a, b, 9a, b). The extension model by Tron & Brun (1991, Fig. 11f) produces the same double rift structure including the additional faults away from the central rifts as our experiment C11 (Fig. 9f, g). Also Keep & McClay (1997) and Schreurs et al. (2006) obtain two rifts with symmetrical extension experiments involving a conveyor or plate base and a brittle-to-viscous ratio of 4 and 6, respectively. A lateral transfer of deformation through the viscous layer, away from the VD is the probable cause of this dual rift arrangement (Michon & Merle 2000; 2003, Fig. 11e). This feature seems to occur in asthenospheric-scale models as well (Vendeville et al. 1987, Fig. 1). A single rift structure may form due to factors as higher strain rates (Keep and McClay 1997; Michon & Merle 2000), asymmetric extension or possibly syn-rift sedimentation (e.g. Brun & Tron 1993, Fig. 11f). The formation of a single or dual rift structure is most likely influenced by the viscosity of the viscous layer as well. Experiments with high brittle-to-viscous ratios thus seem to be highly sensitive to various parameters. Whether the various viscous layer thickness ratios mentioned above are realistic depends on the specific tectonic setting that is simulated, as lithospheric rheological profiles are known to vary considerably in extensional settings (e.g. Brun 1999; Burov 2011; Tetreault & Buiter 2017, see also section 4.7).

4.6. Boundary conditions and boundary effects

Most of our reference experiments, except for the brittle-only plate and conveyor base experiments, develop some degree of normal faulting along the long sidewalls (Fig. 10). In the brittle-only experiments, this may be due to enhanced local stretching of the rubber base (Ackermann 1997), an effect possibly present in the foam base equivalents as well. The rigid sand layer in the brittle-viscous experiments on the other hand is subject to "inertia", i.e. an inability to move and extend as easily as the viscous materials, leaving "gaps" along the sidewalls that take up significant amounts of deformation in the experiment (Zwaan et al. 2017).

Some authors avoid this "inertia" effect by simply ignoring it and focussing on the structures in the centre of the experiment. Others attempt to reduce faulting by applying a viscous layer that does not reach the model sidewalls (Tron & Brun 1991; Schreurs et al. 2006). By narrowing the viscous layer however, the boundaries of the viscous material become rheological contrasts that may trigger faulting themselves, thus causing a new type of boundary effects (e.g. Bonini et al. 1997). This also raises the question what the viscous layer represents in nature, if not a continuous viscous lower crust. Even narrower patches of viscous material, for instance simulating a weak zone in the crust due to magmatism, lead to narrower rift structures (e.g. Brun & Nalpas 1996; Dauteuil et al. 2002) and the seeds in our experiments can be seen as the most extreme exponent of this trend. The width of the structural weakness is also relevant for set-ups involving a rubber base fixed between two base plates (e.g. McClay & White 1995, McClay et al. 2002; Corti et al. 2007; Henza et al. 2010). In such experiments, all deformation occurs above the rubber sheet, with its edges acting as the boundaries of the rift system.

Our results show that the type of confinement along the short edges of the brittle-viscous experiment forms another important factor generating boundary effects. In the foam base

742 experiments, the rubber sheet sidewalls cause little to no additional deformation, yet the sand
743 talus confinement in the rubber base experiments generates significant boundary effects, and
744 enhanced rifting is associated with the plate base and conveyor base confinements. However,
745 the similarity of the structures in the centre of all our reference brittle-viscous experiments (due
746 to the likely dominance of the viscous spreading mechanism under low brittle-viscous coupling
747 conditions) may suggest that, if the short edge boundary effects can be reduced, the type of
748 extension mechanism would be of little influence under our standardized conditions. Therefore
749 we could perhaps have obtained comparable results for brittle-viscous set-ups even without a
750 method to induce deformation directly at the base of the experimental materials: only moving
751 apart the two longitudinal sidewalls may suffice to cause uniform spreading of the viscous layer
752 (e.g. Le Calvez & Vendeville 2002; Autin et al. 2010, 2013; Marques 2012). However, the
753 results of such experiments may again vary with different strain rates, layering and layer
754 thickness, materials, application of sedimentation etc., highlighting the challenges of directly
755 comparing the results from different modelling studies and the need to specify all relevant
756 parameters and boundary conditions, as well as any resulting boundary effects.
757
758 4.7. Recommendations for extension experiments
759
760 Our extension experiments represent different rheological stratifications and extension
761 conditions (Fig. 3), which may serve as a guide for other modelling studies aiming at
762 investigating extension in specific tectonic settings. We calculated a series of rheological
763 profiles for natural cases to allow a direct rheological comparison to the analogue set-ups (Fig.
764 12). We used the rheological values of Table 3 with laboratory flow laws often used for the
765 lower crust and lithospheric mantle (Hirth & Kohlstedt 2003; Rybacki et al. 2006). We varied
766 extension velocity (0.5 to 10 mm/yr) and Moho temperature (550 and 650 °C). The calculations
767 show that extension velocity has a relatively minor influence on the rheological profile with
768 respect to temperature and dry or wet versions of the flow laws. The plots also indicate that our
769 reference brittle-to-viscous ratio of 1:1, although often used in analogue models (Corti et al.
770 2003 and references therein), is quite low (compare Fig. 12a, with Fig. 12b) and may only
771 occur in a relatively wet and hot lithosphere (Fig. 12f). This may for instance be in accordance
772 with the situation in the East African Rift System (Fadaie & Ranalli 1990; Corti 2009), but a 2:1
773 or 3:1 ratio would fit better with the calculations for a normal-temperature lithosphere (Fig. 12b-
774 d). A strong upper mantle, as inferred for (brittle-viscous) plate and conveyor base set-ups, only
775 occurs in a wet cold lithosphere (Fig. 12) or in a completely dry lithosphere (dotted lines in Fig.
776 12), yet the complete absence of hydrous minerals may be unrealistic (Xia & Hao 2010). Note,
777 however, that our strength profile calculations are based on monomineralic flow laws
778 (anorthosite and olivine, Hirth & Kohlstedt 2003; Rybacki et al. 2006), whereas continental
779 rocks are of course polymineralic. Different rheological profiles for natural settings can be
780 obtained by not only varying the thermal gradient, but also by variations in water content,
781 temperature or by simply using other flow laws. We choose lower crust and mantle flow laws
782 (Rybacki et al. 2006 and Hirth & Kohlstedt 2003, respectively) that are fairly recent and neither
783 overly weak nor strong in comparison with other flow laws.
784
785 The rheological calculations highlight that one should carefully consider the various factors that
786 may influence the strength of the lithosphere in a given tectonic setting before selecting a
787 specific experimental set-up. It is also important to stress that although the materials involved
788 may only represent the upper parts of the crust, deeper parts of the lithosphere (basement or
789 mantle) are simulated via the chosen experimental extension mechanism (Fig. 3). This is most
790 evident for brittle-only models that are directly coupled to the set-up (Fig. 10). However, we
791 have shown that for low extension velocity brittle-viscous experiments, that aim at representing
792 a hot lithosphere, any extension mechanism should suffice due to the high degree of
793 decoupling (Fig. 10). This decoupling effect could also allow a simple way to model an oceanic
794 lithosphere, which is generally considered to comprise a brittle oceanic crust and a viscous
795 lithospheric mantle (e.g. Benes & Scott 1996). Note, however, that in such set-ups an imposed
796 weakness is necessary to create any rift structure at all (Fig. 10). Since efforts should be made
797 to keep boundary effects to a minimum, we recommend using the foam base method for such
798 brittle-viscous models (see also section 4.6).

799
800 Our set-ups could be extended to include more layers (three or four-layer lithospheres) (e.g.
801 Corti et al. 2003) and an underlying asthenosphere, that would allow an assessment of the
802 effect of isostatic compensation on a stretching lithosphere. In such set-ups, a strong
803 lithosphere would strongly affect rifting processes (Brun 1999; Corti et al. 2003), whereas in the
804 case of a weak lithosphere (Figs. 3b, e, 12b-d, g, h), the (rising) asthenosphere may have an
805 important impact. The presence of an asthenosphere analogue would also allow the vertical
806 motions associated with a major fault or shear zone in the strong upper mantle (e.g. Vendeville
807 et al. 1987, Fig. 1). In the commonly used plate and conveyor base set-ups such a fault is
808 represented by the VD, yet any associated vertical motions are not simulated. The conveyor
809 belt extension mechanism may not be well suited to crustal-scale models, as the continuous
810 "upwelling" of the plastic sheets resembles a convection cell system, which could be taken to
811 simulate sub-lithospheric mantle behaviour. The conveyor base set-up would therefore be more
812 appropriate for lithospheric-scale models. For crustal-scale wide rift experiments we
813 recommend using a plate base set-up.
814
815 It could also be worthwhile to repeat our experiments with other brittle materials and viscous
816 analogues, which may better capture the behaviour of the lithosphere (overview in Schellart &
817 Strak 2016). The use of temperature-dependent materials would allow the inclusion of
818 temperature effects (e.g. Boutelier & Oncken 2011), which can strongly control rifting as shown
819 by numerical simulations (Tetreault & Buiter, 2017). Furthermore, a next necessary step in
820 modelling rift structures is to include surface processes as well (e.g. Burov & Cloetingh 1997;
821 Bialas & Buck 2009; Zwaan et al. 2017).
822
823 We would like to stress the importance of standardized modelling methods and strict lab
824 procedures (e.g. Klinkmüller et al. 2016). Different handling techniques, laboratory conditions
825 and personal preferences may cause variations in, for instance, sand density (e.g. Krantz
826 1991) or rheology of viscous materials (Rudolf et al. 2015) and can have significant effects on
827 model results (Schreurs et al. 2006, 2016). By means of standardized procedures within a
828 modelling group, these variations can be reduced. Yet reproducing the same model results in
829 different laboratories will probably always remain a challenge (see efforts by Schreurs et al.
830 2006, 2016).
831
832
833 **5. Conclusion**
834
835 We presented a systematic comparison of four setups commonly used for analogue modelling
836 of crustal-scale extension. We examined distributed extension obtained by a foam or rubber
837 base and localised extension by rigid basal plates or conveyor-belt basal sheets. We find that:
838
839 1. Brittle-only experiments are strongly affected by the experimental setup, as the materials
840   are directly coupled to the base of the set-up. Foam base or rubber base experiments
841   therefore undergo distributed deformation and wide rifting, whereas plate base or conveyor
842   base experiments experience localized deformation and narrow rifting.
843 2. Strong boundary effects may occur due to extension-perpendicular contraction effects
844   during stretching of a rubber base (Poisson effect, e.g. Smith & Durney 1992). This may be
845   mitigated by using a high length-to-width ratio for rubber base set-ups.
846 3. Brittle-viscous experiments are less affected by the experimental setup than brittle-only
847   equivalents as the viscous layer acts as a buffer that decouples the brittle parts from the
848   base of the set-up.
849 4. Of the brittle-viscous experiments we tested, the least boundary effects occur for a setup
850   involving a foam base and a stretchable rubber sidewall. This sidewall method could also
851   be applied to a rubber base setup to minimize boundary effects. In contrast, the plate base
852   and conveyor base set-ups may experience major boundary effects along their short
853   sidewalls that may proof difficult to mitigate.
854 5. The poor rift development in our reference brittle-viscous plate base and conveyor base
855   experiments is linked to relatively low brittle-to-viscous thickness ratio and strain rates.

Apart from inserting a structural weakness in the sand, we achieve better localization with higher brittle-to-viscous ratios and higher strain rates, which increase brittle-viscous coupling. High strain rates with reference brittle-to-viscous ratios can also cause intense stretching of the viscous layer and downbending effects, leading to the formation of basins with marginal grabens.

The significant differences between experimental results obtained with the different set-ups, sometimes due to seemingly small differences in, for instance extension velocity or layer thicknesses, indicate the need to accurately specify model parameters and boundary conditions in order to allow meaningful comparisons between (analogue) modelling studies. The combination of rheological stratification and experimental set-up defines the tectonic setting that is investigated. Our set-ups can be applied to study extension of crustal materials in young, weak or old, strong lithospheres with different levels of basement control. Here factors as temperature, extension rate, water content and lithology should be taken into account (Fig. 12). We advise to avoid the conveyor belt method for crustal-scale models.

Finally we recommend that every laboratory standardize its procedures and methods as much as possible in order to minimize variations due to different handling techniques and personal preferences.

### 6.1. Appendix A. Schematic overview of relations between experimental set-ups

Fig. A1 provides an overview of the various set-ups and how these compare to each other by means of extension velocities and shifts of reference frames. All symmetric extension set-ups are different: foam/rubber base experiments (Fig. A1a, b) develop an extension gradient, whereas the plate and conveyor base experiments develop velocity discontinuities (Fig. A1d, e and i, j, respectively). Also the plate and conveyor set-ups are different (e.g. a moving and fixed VD occurs in plate base and conveyor base configurations, respectively, as is revealed after applying a shift of reference frame, Fig A1e, j). Asymmetric extension set-ups differ from their symmetric equivalents as well, but are between themselves, after a shift of reference frame, basically the same (Fig. A1g, l).

### 6.2 Appendix B. Experimental reproducibility

Figs. B1 and B2 show the surface results of repeated experiments in order to evaluate their reproducibility. In most cases, the structures are very similar. Although the boundary effects in P6 and P7 (Fig. B1) do show some variation, the structures in the centre are the same in both cases (no rift). Experiments C4-C6 seem quite different (Fig. B1), but C5 and C6 are tests to reduce boundary effects. As proposed by Tron & Brun (1991), we added sand to confine the short ends of the experiment, but instead of improving the situation this measure increases boundary effects. In C6 (Fig. B1) we added a lubricant (hand soap) between the sides and the model. Since there was no improvement, we aborted the experiment after 120 min. Note that asymmetric brittle-viscous plate base experiment P6 and symmetric brittle-viscous conveyor belt experiment C4 are quite similar, due to viscous decoupling effects. Also asymmetric brittle-only plate/conveyor base experiments P2, C2 and C3 produce the same structures (Fig. B2), since both the plate base and conveyor base set-ups are, after a shift of reference frame, identical in asymmetric extension conditions. The double rift structure in conveyor base experiment C10 is almost identical to the version generated in C11 (Fig. B2), although the curving nature of the normal faults does provide local variations in rift width. High-velocity models P9 and C12 develop very similar structures, although those in the conveyor belt set-up (C12) are better developed than in plate base experiment P9 (Fig. B2). Note that the additional rift basins in C12 are also present in P10, but not very visible due to their less evolved state and the unfavourable lighting conditions.

## 7. Author contribution

The first author, Frank Zwaan, performed the analogue models and composed the first version of the manuscript. Second author and project supervisor Guido Schreurs assisted with the model interpretation and the finalizing of the manuscript. This study was inspired by a collaboration on numerical-analogue comparisons with third author Susanne Buiter, who helped planning and discussing the model series, provided a comparison to natural strength profiles, and helped in finalizing the manuscript.

## 8. Acknowledgements

We would like to express our gratitude to Nicole Schwendener for assisting us with the CT-scanning, Marco Herwegh for providing the necessary financial support to upgrade the experimental apparatus and to the engineers from IPEK Rapperswil (Theodor Wüst, Reto Gwerder, Rudolf Kamber, Michael Ziltener and Christoph Zolliker) for realizing these improvements. We thank John Naliboff and Jürgen Adam for supportive discussions and testing of analysis techniques. This project was funded by the Swiss National Science Foundation (grant no. 200021_147046/1).

## References

Abbate, E., Sagri, M. 1969. Dati e considerazioni sul margine orientale dell'altopiano etiopico nelle province del Tigrai e del Wollo. Bollettino della Società geologica italiana 88, 489–497.

Abdelmalak, M.M., Bulois, C., Mourgues, R., Galland, O., Legland, J.-B., Gruber, C. 2016. Description of new dry granular materials of variable cohesion and friction coefficient: Implications for laboratory modeling of the brittle crust. Tectonophysics 684, 39-51. https://doi.org/10.1016/j.tecto.2016.03.003

Ackermann, R.V. 1997. Spatial distribution of rift related fractures: field observations, experimental modelling, and influence on drainage networks. Unpublished PhD thesis, Rutgers University.

Acocella, V., Faccenna, C., Funiciello, R., Rossetti, F. 1999. Sand-box modelling of basement-controlled transfer zones in extensional domains. Terra Nova 11 (4), 149-156. https://doi.org/10.1046/j.1365-3121.1999.00238.x

Acocella, V., Morvillo, P., Funiciello, R. 2005. What controls relay ramps and transfer faults within rift zones? Insights from analogue models. Journal of Structural Geology 27, 397-408. https://doi.org/10.1016/j.jsg.2004.11.006

Allemand, P., Brun, J.-P., Davy, P., Van der Driessche, J. 1989. Symétrie et asymétrie des rifts et mécanismes d'amincissement de la lithopshère. Bulletin de la Société Géologique de France 8 (3), 445-451. https://doi.org/10.2113/gssgfbull.V.3.445

Allemand, P., Brun, J-.P. 1991. Width of continental rifts and rheological layering of the lithosphere. Tectonophysics 188, 63-69. https://doi.org/10.1016/0040-1951(91)90314-I

Alonso-Henar, J., Schreurs, G., Martinez-Díaz, J.J., Álvarez-Gómez, J.A., Villamor, P. 2015. Neotectonic development of the El Salvador Fault Zone and implications for the deformation in the Central America Volcanic Arc: Insights from 4-D analog modeling experiments. Tectonics 34, 133-151. https://doi.org/10.1002/2014TC003723

Amilibia, A., McClay, K.R., Sàbat, F., Muñoz, J.A., Roca, E. 2005. Analogue Modelling of Inverted Oblique Rift Systems. Geologica Acta 3 (3), 251-271. tp://dx.doi.org/10.1344/105.000001395

Autin, J., Bellahsen, N., Husson, L., Beslier, M.-O., Leroy, S., d'Acremont, E. 2010. Analog models of oblique rifting in a cold lithosphere. Tectonics 29, TC6016. https://doi.org/10.1029/2010TC002671

Autin, J., Bellahsen, N., Leroy, S., Husson, L., Beslier, M.-O., d'Acremont, E. 2013. The role of structural inheritance in oblique rifting: Insights from analogue models and application to the Gulf of Aden. Tectonophysics 607, 51-64. https://doi.org/10.1016/j.tecto.2013.05.041

Bahroudi, A., Koyi, H.A., Talbot, C.J. 2003. Effect of ductile and frictional décollements on style of extension. Journal of Structural Geology 25, 1401-1423. https://doi.org/10.1016/S0191-8141(02)00201-8

Basile, C., Brun, J.-P. 1999. Transtensional faulting patterns ranging from pull-apart basins to transform continental margins: an experimental investigation. Journal of Structural Geology 21, 23-37.

990    https://doi.org/10.1016/S0191-8141(98)00094-7

991

992    Bellahsen, N., Daniel, J-M., Bollinger, L., Burov, E. 2003. Influence of visous layers on the
993    growth of normal faults: insights from experimental and numerical models. Journal of Structural
994    Geology 25, 1471-1485.
995    https://doi.org/10.1016/S0191-8141(02)00185-2

996

997    Bellahsen, N., Daniel, J.M. 2005. Fault reactivation control on normal fault growth: an
998    experimental study. Journal of Structural Geology 27, 769-780.
999    https://doi.org/10.1016/j.jsg.2004.12.003

1000

1001    Benes, V., Scott, S.D. 1996. Oblique rifting in the Havre Trough and its propagation into the
1002    continental margin of New Zealand: Comparison with analogue experiments. Marine
1003    Geophysical Researches 18, 189-201.
1004    https://doi.org/10.1007/BF00286077

1005

1006    Bialas, R.W., Buck, W.R. 2009. How sediment promotes narrow rifting: Application to the Gulf
1007    of California. Tectonics 28, TC4014.
1008    https://doi.org/10.1029/2008TC002394

1009

1010    Bonini, M., Souriot, T., Boccaletti, M., Brun, J.-P. 1997. Successive orthogonal and oblique
1011    extension episodes in a rift zone: Laboratory experiments with application to the Ethiopian Rift.
1012    Tectonics 16 (2), 347-362.
1013    https://doi.org/10.1029/96TC03935

1014

1015    Boutelier, D., Oncken, O. 2011. 3-D thermo-mechanical laboratory modeling of plate-tectonics:
1016    modeling scheme, technique and first experiments. Solid Earth 2, 35-51.
1017    https://doi.org/10.5194/se-2-35-2011

1018

1019    Buck, W.R. 1991. Models of Continental Lithospheric Extension. Journal of Geophysical
1020    Research 96, 20,161-20,178.
1021    https://doi.org/10.1029/91JB01485

1022

1023    Buiter, S.J.H., Huismans, R.S., Beaumont, C. 2008. Dissipation analysis as a guide to mode
1024    selection during crustal extension and implications for the styles of sedimentary basins. Journal
1025    of Geophysical Research 113, B06406.
1026    https://doi.org/10.1029/2007JB005272

1027

1028    Bürgman, R., Dresen, G., 2008. Rheology of the Lower Crust and Upper Mantle: Evidence from
1029    Rock Mechanics, Geodesy, and Field Observations. Annual Review of Earth and Planetary
1030    Sciences 36, 531-67.
1031    https://doi.org/10.1146/annurev.earth.36.031207.124326

1032

1033    Burov, E., Cloetingh, S. 1997. Erosion and rift dynamics: new thermomechanical aspects of
1034    post-rift evolution of extensional basins. Earth and Planetary Science Letters 150, 7-26.
1035    https://doi.org/10.1016/S0012-821X(97)00069-1

1036

1037    Burov, E., Guillou-Frottier, L., d'Acremont, E., Le Pourhiet, L., Cloetingh, S. 2007. Plume head–
1038    lithosphere interactions near intra-continental plate boundaries. Tectonophysics 434, 15-38.
1039    https://doi.org/10.1016/j.tecto.2007.01.002

1040

1041    Burov, E. 2011. Rheology and strength of the lithosphere. Marine and Petroleum Geology
1042    28, 1403-1443.
1043    https://doi.org/10.1016/j.marpetgeo.2011.05.008

1044

1045  Brun, J.-P. 1999. Narrow rifts versus wide rifts: inferences for the mechanics of rifting from
1046  laboratory experiments. Philosophical Transactions of the Royal Society London A 357, 695-
1047  712.
1048  https://doi.org/10.1098/rsta.1999.0349
1049
1050
1051  Brun, J.-P., Tron, V. 1993. Development of the North Viking Graben: inferences from laboratory
1052  modelling. Sedimentary Geology 86, 31-51.
1053  https://doi.org/10.1016/0037-0738(93)90132-O
1054
1055  Brun, J.-P., Nalpas, T. 1996. Graben inversion in nature and experiments. Tectonics 15, 677-
1056  687.
1057  https://doi.org/10.1029/95TC03853
1058
1059  Cagnard, F., Brun, J.-P., Gapais, D. 2006. Modes of thickening of analogue weak lithospheres.
1060  Tectonophysics 421, 145-160. https://10.1016/j.tecto.2006.04.016
1061
1062  Calignano, E., Sokoutis, D., Willingshofer, E., Gueydan, F., Cloetingh, S. 2015. Asymmetric vs.
1063  symmetric deep lithospheric architecture of intra-plate continental orogens. Earth and Planetary
1064  Science Letters 424, 38–50.
1065  http://dx.doi.org/10.1016/j.epsl.2015.05.022
1066
1067  Carlo AG (Carlo Bernasconi AG, Switzerland) 2018.
1068  Company website: www.carloag.ch
1069
1070  Casas, A. M., D. Gapais, T. Nalpas, K. Besnard, and T. Román‐Berdiel (2001), Analogue
1071  models of transpressive systems, Journal of Structural Geology, 23, 733–743,
1072  http://dx.doi.org/10.1016/S0191-8141(00)00153-X
1073
1074  Chemenda, A., Déverchère, J., Calais, E. 2002. Three-dimensional laboratory modelling of
1075  rifting: application to the Baikal Rift, Russia. Tectonophysics 356, 253-273.
1076  https://doi.org/10.1016/S0040-1951(02)00389-X
1077
1078  Chorowicz, J., Collet, B., Bonavia, F., Korme, T. 1999. Left-lateral strike- slip tectonics and
1079  gravity induced individualisation of wide continental blocks in the western Afar margin. Eclogae
1080  geologicae Helvetiae 92, 149–158.
1081  https://www.e-periodica.ch/cntmng?pid=egh-001:1999:92::596
1082
1083  Clifton, A.E., Schlische, R.W. 2001. Nucleation, growth and linkage of faults in oblique rift
1084  zones: Results from experimental clay models and implications for maximum fault size.
1085  Geology 29 (5), 455-458.
1086  https://doi.org/10.1130/0091-7613(2001)029<0455:NGALOF>2.0.CO;2
1087
1088  Cobbold, P.R., Quinquis, H., 1980. Development of sheath folds in shear regimes. Journal of
1089  Structural Geology 2, 119–126.
1090
1091  Colletta, B., Letouzey, J., Pinedo, R., Ballard, J.F., Balé, P. 1991. Computerized X-ray
1092  tomography analysis of sandbox models: Examples of thin-skinned thrust systems. Geology 19,
1093  1063-1067.
1094  https://doi.org/10.1130/0091-7613(1991)019<1063:CXRTAO>2.3.CO;2
1095
1096  Corti, G. 2009. Continental rift evolution: From rift initiation to incipient break-up in the Main
1097  Ethiopian Rift, East Africa. Earth-Science Reviews 96, 1-53.
1098  https://doi.org/10.1016/j.earscirev.2009.06.005
1099

1100 Corti, G., Bonini, B., Conticelli, S., Innocenti, F., Manetti P., Sokoutis, D. 2003. Analogue
1101 modelling of continental extension: a review focused on the relations between the patterns of
1102 deformation and the presence of magma.
1103 https://doi.org/10.1016/S0012-8252(03)00035-7

1105 Corti, G., Van Wijk, J., Cloetingh, S., Morley, C.K. 2007. Tectonic inheritance and continental
1106 rift architecture: Numerical and analogue models of the East African Rift system. Tectonics 26,
1107 TC6006.
1108 https://doi.org/10.1029/2006TC002086

1110 Corti, G., Agostini, A., Keir, d., Van Wijk, J., Bastow, I.D., Ranalli, G. 2015. Magma-induced
1111 axial subsidence during final-stage rifting: Implications for the development of seaward-dipping
1112 reflectors. Geosphere 11 (3), 563-571.
1113 https://doi.org/10.1130/GES01076.1

1115 Dauteuil, O., Brun, J.-P. 1993. Oblique rifting in a slow-spreading ridge. Nature 361, 145-148.
1116 https://doi.org/10.1038/361145a0

1118 Dauteuil, O., Bourgeois, O., Mauduit, T. 2002. Lithosphere strength controls oceanic transform
1119 structure: insights from analogue models. Geophysical Journal International 150, 706-714.
1120 10.1046/j.1365-246X.2002.01736.x

1122 Dixon, J.M., Summers, J.M., 1985. Recent developments in centrifuge modelling of tectonic
1123 processes: equipment, model construction techniques and rheology of model materials. J.
1124 Struct. Geol. 7, 83–102.

1126 Dooley, T.P., Schreurs, G. 2012. Analogue modelling of intraplate strike-slip tectonics: A review
1127 and new experimental results. Tectonophysics 574-575, 1-71.
1128 http://dx.doi.org/10.1016/j.tecto.2012.05.030

1130 Eisenstadt, G., Sims, D. 2005. Evaluating sand and clay models: do rheological differences
1131 matter? Journal of Structural Geology 27, 1399–1412.
1132 https://doi.org/10.1016/j.jsg.2005.04.010

1134 Elmohandes, S.-E. 1981. The Central European Graben System: Rifting Imitated by Clay
1135 Modelling. Tectonophysics 73, 69-78.
1136 https://doi.org/10.1016/0040-1951(81)90174-8

1138 Fadaie, K., Ranalli, G. 1990. Rheology of the lithosphere in the East African Rift System.
1139 Geophysical Journal International 102, 445-453.
1140 https://doi.org/10.1111/j.1365-246X.1990.tb04476.x

1142 Fort, X., Brun, J.-P., Chauvel F. 2004. Salt tectonics on the Angolan margin, synsedimentary
1143 deformation processes. AAPG Bulletin 88 (11), 1523-1544.
1144 https://doi.org/10.1306/06010403012

1146 Gartrell, A.P. 1997. Evolution of rift basins and low-angle detachments in multilayer analog
1147 models. Geology 25 (7), 615-618.
1148 https://doi.org/10.1130/0091-7613(1997)025<0615:EORBAL>2.3.CO;2

1150 Handin, J., 1969. On the Coulomb–Mohr failure criterion. Journal of Geophysical Research 74,
1151 5343–5348.
1152 https://doi.org/10.1029/JB074i022p05343

1154 Henza, A.A., Withjack, M.O., Schlische, R.W. 2010. Normal-fault development during two
1155 phases of non-coaxial extension: An experimental study. Journal of Structural Geology 32,
1156 1656-1667.

1157    https://doi.org/10.1016/j.jsg.2009.07.007
1158
1159    Hirth, G. and D.L. Kohlstedt (2003), Rheology of the upper mantle and the mantle wedge: A
1160    view from the experimentalists. In: Eiler, J. (ed), Inside the Subduction Factory. American
1161    Geophysical Union Geophysical Monograph 138, 83-105.
1162    https://doi.org/10.1029/138GM06
1163
1164    Hubbert, M.K. 1937. Theory of scaled models as applied to the study of geological structures.
1165    Geological Society of America Bulletin 48, 1459-1520.
1166    https://doi.org/10.1130/GSAB-48-1459
1167
1168    Hubbert, M.K., 1951. Mechanical basis for certain familiar geological structures.
1169    Geological Society of America Bulletin 62, 355-372.
1170    https://doi.org/10.1130/0016-7606(1951)62[355:MBFCFG]2.0.CO;2
1171
1172    Jaeger, J.C., Cook, N.G.W., 1976. Fundamentals of Rock Mechanics. Chapman & Hall, Wiley,
1173    New York.
1174
1175    Keep, M., McClay, K.R. 1997. Analogue modelling of multiphase rift systems. Tectonophysics
1176    273, 239
1177    https://doi.org/10.1016/S0040-1951(96)00272-7
1178
1179    Klinkmüller, M., Schreurs, G., Rosenau, M., Kemnitz, H. 2016. Properties of granular analogue
1180    model materials: A community wide survey. Tectonophysics 684, 23-38.
1181    http://dx.doi.org/10.1016/j.tecto.2016.01.017
1182
1183    Konstantinovskaya, E.A., Harris, L.B., Poulin, J., Ivanov, G.M. 2007. Transfer zones and fault
1184    reactivation in inverted rift basins: Insights from physical modelling. Tectonophysics 441, 1-26.
1185    https://10.1016/j.tecto.2007.06.002
1186
1187    Kranzt, R.W., 1991. Measurements of friction coefficients and cohesion for faulting and fault
1188    reactivation in laboratory models using sand and sand mixtures. Tectonophysics 188, 203-207.
1189    https://doi.org/10.1016/0040-1951(91)90323-K
1190
1191    Le Calvez, J.H., Vendeville, B.C. 2002. Experimental designs to model along-strike fault
1192    interaction. Journal of the Virtual Explorer 7, 1-17.
1193    https://doi.org/10.3809/jvirtex.2002.00043
1194
1195    Mart, Y., Dauteuil, O. 2000. Analogue experiments of propagation of oblique rifts.
1196    Tectonophysics 316, 121-132.
1197    https://doi.org/10.1016/S0040-1951(99)00231-0
1198
1199    Marques, F.O. 2012. Transform faults orthogonal to rifts: Insights from fully gravitational
1200    physical models. Tectonophysics 526-529, 42-47.
1201    https://doi.org/10.1016/j.tecto.2011.08.018
1202
1203    McClay, K.R., White, M.J. 1995. Analogue modelling of orthogonal and oblique rifting. Marine
1204    and Petroleum Geology 12 (2), 137-151.
1205    https://doi.org/10.1016/0264-8172(95)92835-K
1206
1207    McClay, K.R., Dooley, T., Whitehouse, P., Mills, M. 2002. 4-D evolution of rift systems: Insights
1208    from scaled physical models. AAPG Bulletin 86, 935-959.
1209    http://www.searchanddiscovery.com/documents/mcclay03/images/mcclay03.pdf
1210
1211    Michon, L., Merle, O. 2000. Crustal structures of the Rhinegraben and the Massif Central
1212    grabens: An experimental approach. Tectonics 19 (5), 896-904.
1213    https://doi.org/10.1029/2000TC900015

1214

1215 Michon, L., Merle, O. 2003. Mode of lithospheric extension: Conceptual models from analogue
1216 modeling. Tectonics 22, 1028.
1217 https://doi.org/10.1029/2002TC001435
1218

1219 Montanari, D., Agostini, A., Bonini, M., Corti, G., Del Ventisette, C. 2017. The Use of Empirical
1220 Methods for Testing Granular Materials in Analogue Modelling. Materials 10, 635
1221 https://dx.doi.org/10.3390%2Fma10060635
1222

1223 Molnar, N.E., Cruden, A.R., Betts, P.G. 2017. Interactions between propagating rotational rifts
1224 and linear rheological heterogeneities: Insights from three-dimensional laboratory experiments.
1225 Tectonics 36, 420-443.
1226 https://doi.org/10.1002/2016TC004447
1227

1228 Mulugeta, G. 1988. Squeeze box in the centrifuge. Tectonophysics 148, 323-335.
1229 https://doi.org/10.1016/0040-1951(88)90139-4
1230

1231 Naliboff, J., Buiter, S.J.H. 2015. Rift reactivation and migration during multiphase extension.
1232 Earth and Planetary Science Letters 421, 58–67.
1233 http://dx.doi.org/10.1016/j.epsl.2015.03.050
1234

1235 Nalpas, T., Brun, J.-P. 1993. Salt flow and diapirism related to extension at crustal scale.
1236 Tectonophysics 228, 349-362.
1237 https://doi.org/10.1016/0040-1951(93)90348-N
1238

1239 Panien, M., Schreurs, G, Pfiffner, A. 2005. Sandbox experiments on basin inversion: testing the
1240 influence of basin orientation and basin fill. Journal of Structural Geology 27, 433-445.
1241 https://doi.org/10.1016/j.jsg.2004.11.001
1242

1243 Panien, M., Schreurs, G, Pfiffner, A. 2006. Mechanical behaviour of granular materials used in
1244 analogue modelling: insights from grain characterisation, ring-shear tests and analogue
1245 experiments. Journal of Structural Geology 28, 1710-1724.
1246 https://doi.org/10.1016/j.jsg.2006.05.004
1247

1248 Philippon, M., Willingshofer, E., Sokoutis, D., Corti, G., Sani, F., Bonini, M., Cloetingh, S. 2015.
1249 Slip re-orientation in oblique rifts. Geology 43, 147-150.
1250 https://doi.org/10.1130/G36208.1
1251

1252 Ramberg, H. 1981. Gravity, Deformation and the Earth's Crust. Academic Press, London.
1253

1254 Román-Berdiel, T., Aranguren. A., Cuevas, J., Tubía, J.M., Gaipas, D., Brun, J-.P. 2000.
1255 Experiments on granite intrusion in transtension. In: Vendeville, B., Mart, Y., Vigneresse, J-.L.
1256 (eds) Salt, Shale and Igneous Diapirs in and around Europe. Geological Society, London,
1257 Special Publications 174, 21-42.
1258 https://doi.org/10.1144/GSL.SP.1999.174.01.02
1259

1260 Rudolf, M., Boutelier, D., Rosenau, M., Schreurs, G., Oncken, O. 2015. Rheological benchmark
1261 of silicone oils used for analog modeling of short- and long-term lithospheric deformation.
1262 Tectonophysics 684, 12-22.
1263 http://dx.doi.org/10.1016/j.tecto.2015.11.028
1264

1265 Rybacki, E., Gottschalk, M., Wirth, R., Dresen, G. (2006), Influence of water fugacity and
1266 activation volume on the flow properties of fine-grained anorthite aggregates. Journal of
1267 Geophysical Research 111 (B3)
1268 https://doi.org/10.1029/2005JB003663
1269

1270 Saria, E., Calais, E., Stamps, D.S., Delvaux, D., Hartnady, C.J.H. 2014. Present-day
1271 kinematics of the East African Rift. Journal of Geophysical Research. Solid Earth 119, 3584-
1272 3600.
1273 https://doi.org/10.1002/2013JB010901
1274
1275 Saunders, A.D., Storey, M., Kent, R.W., Norry, M.J. 1992. Consequences of plume-lithosphere
1276 interactions. Geological Society, London, Special Publications 68, 41-60.
1277 https://doi.org/10.1144/GSL.SP.1992.068.01.04
1278
1279 Schellart, W.P., Lister, G.S., Jessell, M.W. 2002. Analogue modelling of asymmetrical back-arc
1280 extension. In: Schellart, W.P., Passchier, C. (eds.) Analogue modelling of large-scale tectonic
1281 processes. Journal of the Virtual Explorer 7, 25-42.
1282 https://doi.org/10.3809/jvirtex.2002.00046
1283
1284 Schellart, W.P., Jessell, M.W., Lister, G.S. 2003. Asymmetric deformation in the backarc region
1285 of the Kuril arc, northwest Pacific: New insights from analogue modelling. Tectonics, 22 (5),
1286 1047.
1287 https://doi.org/10.1029/2002TC001473
1288
1289 Schellart, W.P., Strak, V. 2016. A review of analogue modelling of geodynamic processes:
1290 Approaches, scaling, materials and quantification, with an application to subduction
1291 experiments.  Journal of Geodynamics 100, 7-32.
1292 https://doi.org/10.1016/j.jog.2016.03.009
1293
1294 Schlagenhauf, A., Manighetti, I., Malavieille, J., Dominguez, S., 2008. Incremental growth of
1295 normal faults: Insights from a laser-equipped analog experiment. Earth and Planetary Science
1296 Letters 273, 299–311
1297 https://doi.org/10.1016/j.epsl.2008.06.042
1298
1299 Schreurs, G., Colletta, B. 1998. Analogue modelling of faulting in zones of continental
1300 transpression and transtension. Geological Society, London, Special Publications, 135, 59-79.
1301 https://doi.org/10.1144/GSL.SP.1998.135.01.05
1302
1303 Schreurs, G., Buiter, S.J.H., Boutelier, D., Corti, G., Costa, E., Cruden, A.R., Daniel, J.-M., Hoth,
1304 S., Koyi, H.A., Kukowski, N., Lohrmann, J., Ravaglia, A., Schlische, R.W., Withjack, M.O.,
1305 Yamada, Y., Cavozzi, C., Delventisette, C., Brady, J.A.E., Hoffmann-Rothe, A., Mengus, J.-M.,
1306 Montanari, D., Nilforushan, F. 2006. Analogue benchmarks of shortening and extension
1307 experiments. In: Buiter, S.J.H., Schreurs, G. (eds.) Analogue and Numerical Modelling of
1308 Crustal-Scale Processes. Geological Society, London, Special Publications 253, 1-27.
1309 https://doi.org/10.1144/GSL.SP.2006.253.01.01
1310
1311 Schreurs, G., Buiter, S.J.H., Boutelier, J., Burbery, C., Callot, J.-P. Cavozzi, C., Cerca, M.,
1312 Chen, J.-H., Cristallini, E., Cruden, A.R., Cruz, L., Daniel, J.-M., Da Poian, G., Garcia, V.H.,
1313 Gomes, C.J.S., Grall, C., Guillot, Y., Guzmán, C., Hidayah, T.N., Hilley, G., Klinkmüller. M.,
1314 Koyi, H.A., Lu, C.-Y., Maillot, B., Meriaux, C., Nilfouroushan, F., Pan, C.-C., Pillot D., Portillo, R.,
1315 Rosenau, M, Schellart, W.P., Schlische, R.W., Take, A., Vendeville, B., Vergnaud, M., Vettori,
1316 M., Wang, S.-H., Withjack, M.O., Yagupsky, D., Yamada, Y. 2016. Benchmarking analogue
1317 models of brittle thrust wedges. Journal of Structural Geology 92, 116-139.
1318 https://doi.org/10.1016/j.jsg.2016.03.005
1319
1320 Serra, S., Nelson, R.A. 1988. Clay modeling of rift asymmetry and associated structures.
1321 Tectonophysics 153, 307-312.
1322 https://doi.org/10.1016/0040-1951(88)90023-6
1323
1324 Shinevar, W.J., Behn, M.D., Hirt, G., 2015. Compositional dependence of lower crustal
1325 viscosity. Geophysical Research Letters 42, 8333–8340.
1326 https://doi.org/10.1002/2015GL065459

1327
1328 Smith, J.V., Durney, D.W. Experimental formation of brittle structural assemblages in oblique
1329 divergence. Tectonophysics 216, 235-253.
1330 https://doi.org/10.1016/0040-1951(92)90399-Q
1331
1332 Sun., Z., Zhong, Z., Keep, M., Zhou, D., Cai, D., Li, X., Wu, S., Jiang, J. 2009. 3D analogue
1333 modelling of the South China Sea: A discussion on breakup pattern. Journal of Asian Earth
1334 Sciences 34, 544-556.
1335 https://doi.org/10.1016/j.jseaes.2008.09.002
1336
1337 Tetreault, J.L., Buiter, S.J.H. 2017. The influence of extension rate and crustal rheology on the
1338 evolution of passive margins from rifting to break-up
1339 https://doi.org/10.1016/j.tecto.2017.08.029
1340
1341 Tron, V. Brun, J.-P. 1991, Experiments on oblique rifting in brittle-ductile systems.
1342 Tectonophysics 188, 71-88.
1343 https://doi.org/10.1016/0040-1951(91)90315-J
1344
1345 Twiss, R.J., Moores, E.M., 1992. Structural Geology. W.H. Freeman and Company, New York
1346
1347 Ustaszewski, K., Schumacher, M.E., Schmid, S.M., Nieuwland, D. 2005. Fault reactivation in
1348 brittle–viscous wrench systems–dynamically scaled analogue models and application to the
1349 Rhine–Bresse transfer zone. Quaternary Science Reviews 24, 365-382.
1350 https://doi.org/10.1016/j.quascirev.2004.03.015
1351
1352 Vendeville, B., Cobbold, P.R., Davy, P., Brun, J.-P., Choukroune, P. 1987. Physical models of
1353 extensional tectonics at various scales. In: Coward, M.P., Dewey, J.F., Hancock, P.L. (eds.)
1354 Continental Extensional Tectonics. Geological Society, London, Special Publications 28, 95-
1355 107.
1356 https://doi.org/10.1144/GSL.SP.1987.028.01.08
1357
1358 Venkat-Ramani, M., Tikoff, B. 2002. Physical models of transtensional folding. Geology 30,
1359 523-526.
1360 https://doi.org/10.1130/0091-7613(2002)030<0523:PMOTF>2.0.CO;2
1361
1362 Weijermars, R. 1986. Flow behaviour and physical chemistry of bouncing putties and related
1363 polymers in view of tectonic laboratory applications. Tectonophysics 124, 325-358. https://
1364 10.1016/0040-1951(86)90208-8
1365
1366 Weijermars, R., Schmeling, H. 1986. Scaling of Newtonian and non-Newtonian fluid dynamics
1367 without inertia for quantitative modelling of rock flow due to gravity (including the concept of
1368 rheological similarity). Physics of Earth and Planetary Interiors 43, 316-330.
1369 https://doi.org/10.1016/0031-9201(86)90021-X
1370
1371 Xia, Q.K., Hao, Y.T. 2010. The distribution of water in the continental lithospheric mantle and its
1372 implications for the stability of continents. Chinese Science Bulletin 58, 3897-3889.
1373 https://doi.org/10.1007/s11434-013-5949-1
1374
1375 Zulauf, J, Zulauf, G. 2004. Rheology of plasticine used as rock analogue: the impact of
1376 temperature, composition and strain. Journal of Structural Geology 26, 725–737.
1377 https://doi.org/10.1016/j.jsg.2003.07.005
1378
1379 Zwaan, F., G. Schreurs, J. Naliboff, Buiter, S.J.H. 2016. Insights into the effects of oblique
1380 extension on continental rift interaction from 3D analogue and numerical models.
1381 Tectonophysics 693, 239-260.
1382 https://doi.org/10.1016/j.tecto.2016.02.036
1383

1384  Zwaan, F., Schreurs, G. 2017. How oblique extension and structural inheritance influence rift
1385  segment interaction: Insights from 4D analog models. Interpretation 5 (1), SD119-SD138.
1386  https://doi.org/10.1190/INT-2016-0063.1
1387
1388  Zwaan, F., Schreurs, G. Adam, J., 2017. Effects of sedimentation on rift segment evolution and
1389  rift interaction in orthogonal and oblique extensional settings: Insights from analogue models
1390  analysed with 4D X-ray computed tomography and digital volume correlation techniques.
1391  Global and Planetary Change.
1392  https://doi.org/10.1016/j.gloplacha.2017.11.002
1393
1394
1395
1396
1397
1398
1399
1400
1401

**Table captions**

Table 1. Material properties

| Granular materials | Quartz sand[a] | Corundum sand[b] |
|---|---|---|
| Grain size range | 60-250 µm | 88-175 µm |
| Density (specific)[c] | 2650 kg/m$^3$ | 3950 kg/m$^3$ |
| Density (sieved) | 1560 kg/m$^3$ | 1890 kg/m$^3$ |
| Angle of internal peak friction | 36.1˚ | 37˚ |
| Angle of dynamic-stable friction | 31.4˚ | 32˚ |
| Cohesion | 9 ± 98 Pa | 39 ± 10 Pa |
| **Viscous material** | **PDMS/corundum sand mixture[a]** | |
| Pure PDMS density (specific)[a] | 0.965 kg/m$^3$ | |
| Weight ratio PDMS : corundum sand | 0.965 kg : 1.00 kg | |
| Mixture density | ca. 1600 kg/m$^3$ | |
| Viscosity[d] | ca. 1.5·10$^5$ Pa·s | |
| Type | near-Newtonian (n = 1.05)[e] | |

[a] Quartz sand, pure PDMS and viscous mixture characteristics after Zwaan et al. (2016)
[b] Corundum sand characteristics after Panien et al. (2006)
[c] Specific densities of quartz and corundum sands after Carlo AG (2018)
[d] The viscosity value holds for model strain rates < 10$^{-4}$ s$^{-1}$
[e] Stress exponent n (dimensionless) represents sensitivity to strain rate

1415  Table 2. List of models
1416

| Base | Model | Layering Type | Thickness (brittle/viscous) | Seed | Extension Type | Velocity | Shown in: |
|---|---|---|---|---|---|---|---|
| Foam base (F series) | **F1** | Brittle only | 40/- mm | No | Symmetric | 8 mm/h | Fig. 4 |
| | F2 | | | | | 8 mm/h | |
| | F3 | | | Seed | | 8 mm/h | |
| | **F4[CT]** | | | | | 8 mm/h | Fig. 4 |
| | **F5** | Brittle-viscous | 40/40 mm | No | | 8 mm/h | Fig. 5 |
| | F6 | | | | | 8 mm/h | |
| | **F7[CT]** | | | Seed | | 8 mm/h | Fig. 5 |
| Rubber base (R series) | R1[a] | Brittle only | 40/- mm | No seed | Symmetric | 1st phase: 8 mm/h 2nd phase: 40 mm/h | Fig. 6 |
| | R2[b] | | | Seed | | 10 mm/h | |
| | R3[b] | | | | | 20 mm/h | |
| | R4[CT, b,] | | | | | 20 mm/h | |
| | **R5[CT, b]** | | | | | 10 mm/h | Fig. 6 |
| | R6[CT, d] | | | | | 20 mm/h | |
| | **R7[a]** | Brittle-viscous | 40/40 mm | No seed | | 1st phase: 8 mm/h 2nd phase: 40 | Fig. 7 |
| | **R8** | | | Seed | | 8 mm/h | Fig. 7 |
| | **R9** | | | No seed | | 80 mm/h | Fig. 7 |
| | **R10** | | | | | 480 mm/h | Fig. 7 |
| Plate base (P series) | **P1** | Brittle only | 40/- mm | No seed | Symmetric | 8 mm/h | Fig. 8 |
| | **P2** | | | | Asymmetric | 8 mm/h | Fig. 8 |
| | **P3** | Brittle-viscous | 40/40 mm | | Symmetric | 8 mm/h | |
| | P4 | | | | | 2 mm/h | |
| | P5 | | | | | 40 mm/h | |
| | P6 | | | | | 8 mm/h | |
| | **P7** | | | | Asymmetric | 8 mm/h | Fig. 8 |
| | P8[e] | | 20/20 mm | | Symmetric | 2 mm/h | Fig. 8 |
| | **P9[e]** | | | | | 80 mm/h | Fig. 8 |
| | **P10** | | 40/40 mm | Seed | | 8 mm/h | Fig. 8 |
| Conveyor base (C series) | **C1** | Brittle only | 40/- mm | No seed | Symmetric | 40 mm/h | Fig. 9 |
| | C2 | | | | | 40 mm/h | |
| | **C3** | | | | Asymmetric | 40 mm/h | Fig. 9 |
| | **C4** | Brittle-viscous | 40/40 mm | | Symmetric | 8 mm/h | Fig. 9 |
| | C5[f] | | | | | 8 mm/h | |
| | C6[f] | | | | | 8 mm/h | |
| | **C7** | | 40/20 mm | | | 8 mm/h | Fig. 9 |
| | **C8** | | | | | 8 mm/h | Fig. 9 |
| | C9 | | 40/10 mm | | | 80 mm/h | |
| | C10 | | | | | 40 mm/h | |
| | **C11[CT]** | | | | | 40 mm/h | Fig. 9 |
| | C12[e] | | 20/20 mm | | | 80 mm/h | |

1417
1418  Bold        Shown in this article
1419  CT          CT-scanned models
1420  a           Two-phase model with 40 mm of extension at 8 mm/h followed by 20 mm of extension at 40 mm/h
1421  b           Initial model width 25 cm instead of 30 cm
1422  c           54 mm total extension; rubber sheet ripped partly after ca. 2 h (40 mm extension)
1423  d           Total extension: 60 mm
1424  e           Models with a total 40 mm thickness (20 mm brittle, 20 mm viscous) and 20 mm total extension
1425  f           Attempt to reduce boundary effects (see text and Fig. B2 in Appendix B for details)
1426

1427    Table 3. Scaling parameters
1428

| | General parameters | | | Brittle upper crust | | Ductile lower crust | | Dynamic scaling values | |
|---|---|---|---|---|---|---|---|---|---|
| | Gravitational acceleration g $(m/s^2)$ | Upper crustal thickness h (m) | Extension velocity v (m/s) | Density $\rho$ $(kg/m^3)$ | Cohesion C (Pa) | Density $\rho$ $(kg/m^3)$ | Viscosity $\eta$ (Pa·s) | Ramberg number $R_m$ | Brittle stress ratio $R_s$ |
| Model (reference) | 9.81 | $4 \cdot 10^{-2}$ | $2.2 \cdot 10^{-6}$ | 1560 | 9 | 1600 | $1.5 \cdot 10^5$ | 75 | 68 |
| Nature | 9.81 | $2 \cdot 10^4$ | $1.5 \cdot 10^{-10}$ | 2800 | $8 \cdot 10^6$ | 2870 | $1 \cdot 10^{21}$ | 75 | 68 |

1429
1430
1431

1432    Table 4. Overview of links between our analogue set-ups, the resulting structures observed in
1433    our experiments and their natural analogues
1434

| Type | Layering | Extension velocity | Brittle-viscous ratio used | Coupling observed in experiments | Natural analogue | Structural style observed in experiments |
|---|---|---|---|---|---|---|
| Foam/Rubber | Brittle | Slow | - | Very high coupling of brittle layer with substratum | Strong ductile lower crust (Fig. 3a) | No seed: wide rifting (Fig. 10a, a') |
| | | | | | | Seed: wide rifting with small localized graben (Fig. 10b, b') |
| | | | | | | NB: Rubber base: conjugate faults may occur! (Fig. 10e, e', f, f') |
| | Brittle-viscous | Slow | 1:1 | Low coupling between all components* | Weak, hot lithosphere (strong mantle absent) (Fig. 3b) | No seed: only boundary effects (Fig. 10c, c') |
| | | | | | | Seed: localized rifting (Fig. 10d, d') |
| | | Fast | 1:1 | High coupling between all components | Strong ductile lower crust, but weak ductile upper mantle (Fig. 3e) | No seed: wide rifting (Fig. 10m, m') |
| | | | | | | Seed: wide rifting with a localized graben (e.g. Zwaan et al. 2016) |
| Plate/Conveyor belt | Brittle | Slow | - | Very high coupling of brittle layer with substratum | Cold lithosphere; Fault in (thick) brittle crust or brittle mantle (Fig. 3c). | Narrow rifting (Fig. 10i, i', j, j') |
| | Brittle-viscous | Slow | 1:1 | Low coupling between all components* | Hot lithosphere with thick ductile lower crust above brittle upper mantle (Fig. 3d) | No seed: wide rifting (Fig. 10k, k) |
| | | | | | | Seed: wide rifting with small localized graben (Fig. 10l, l') |
| | | | 4:1 | High coupling between all components* | Cold lithosphere with thin ductile lower crust above brittle upper mantle (Fig 3h) | No seed: Wide (double) rifting (Fig. 10o, o') |
| | | | | | | Seed: Not known |
| | | Fast | 1:1 | Very high coupling between all components* | Hot lithosphere with thick ductile lower crust above brittle upper mantle (Fig. 3f) | No seed: Downbending basin (Fig. 10m, m') |
| | | | | | | Seed: Not known |
| | | | 4:1 | Very high coupling between all components* | Cold lithosphere with thin ductile lower crust above brittle upper mantle (Fig. 3h) | Narrow (double) rifting (Fig. 10p, p') |
| | | | | | | Seed: Not known |

1435
1436    **(*) all components: all parts of the set-up, i.e. the sand layer, viscous layer and**
1437    **substratum (or base of the set-up)**

1438 **Figures + captions**
1439
1440
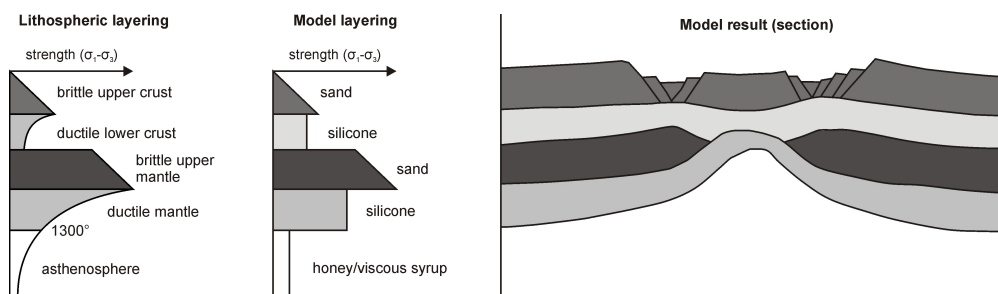
1441
1442
1443 Fig. 1. Example of model layering to simulate extension in a stable four-layer lithosphere. Left:
1444 strength profile of the natural example, with a brittle upper crust, a ductile lower crust, a strong
1445 brittle upper mantle and a ductile lower mantle that blends into the underlying asthenosphere at
1446 a temperature of 1300 ˚C. Middle: model materials representing the various layers: sand for the
1447 brittle parts of the lithosphere, viscous silicone (mixtures) for the ductile crust and mantle. The
1448 asthenosphere is simulated with a honey or viscous syrup. Right: cross-section at the end of
1449 the extension experiment. Adapted from Allemand & Brun (1991) with permission from Elsevier.
1450
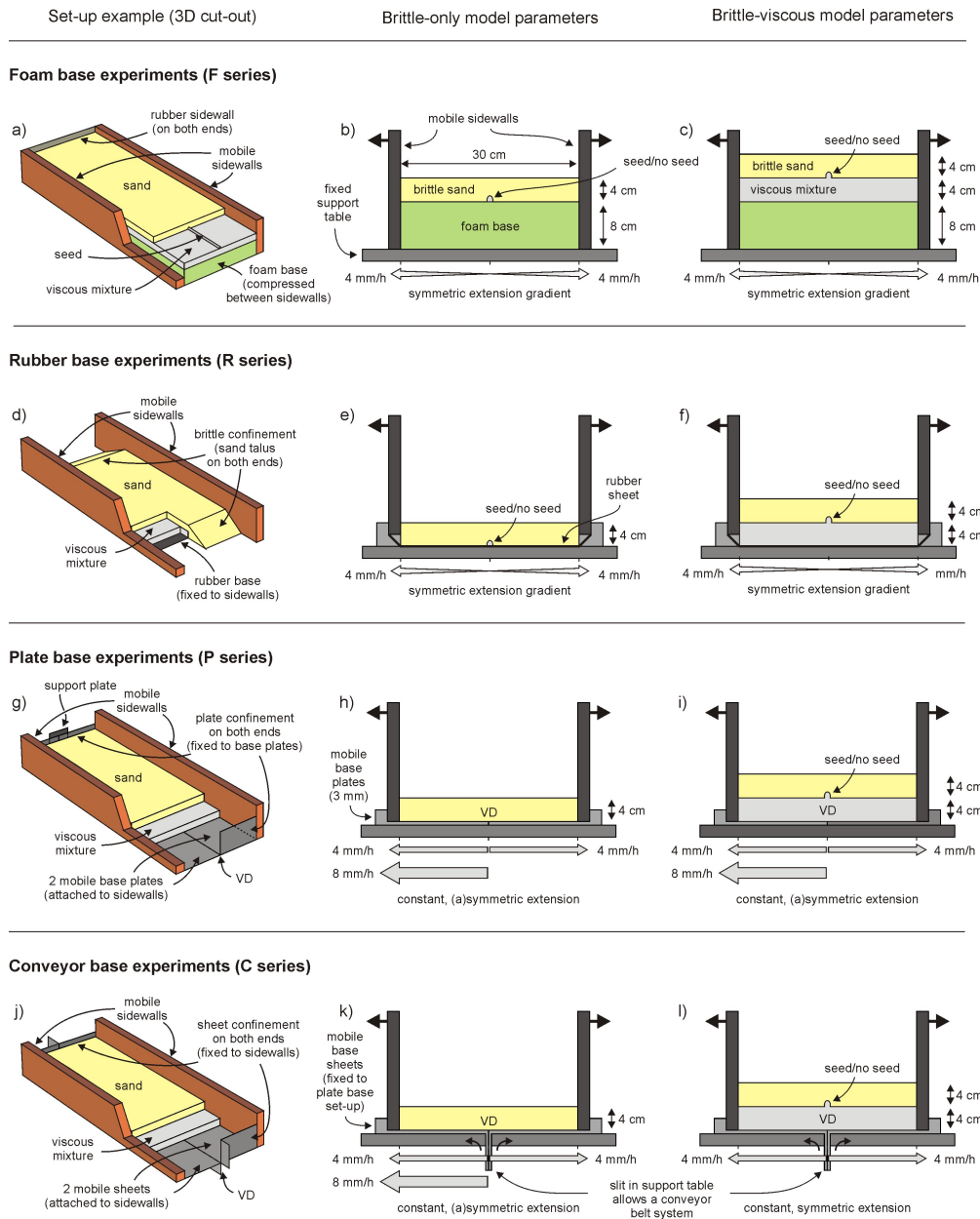
Fig. 2. Reference set-ups tested for this paper. See Table 2 for a complete overview of the specific model parameters applied in this study. Note that the 3D cut-out views show examples of reference set-ups with brittle-viscous layering. VD: velocity discontinuity. For details on the additional set-ups, see Table 2.
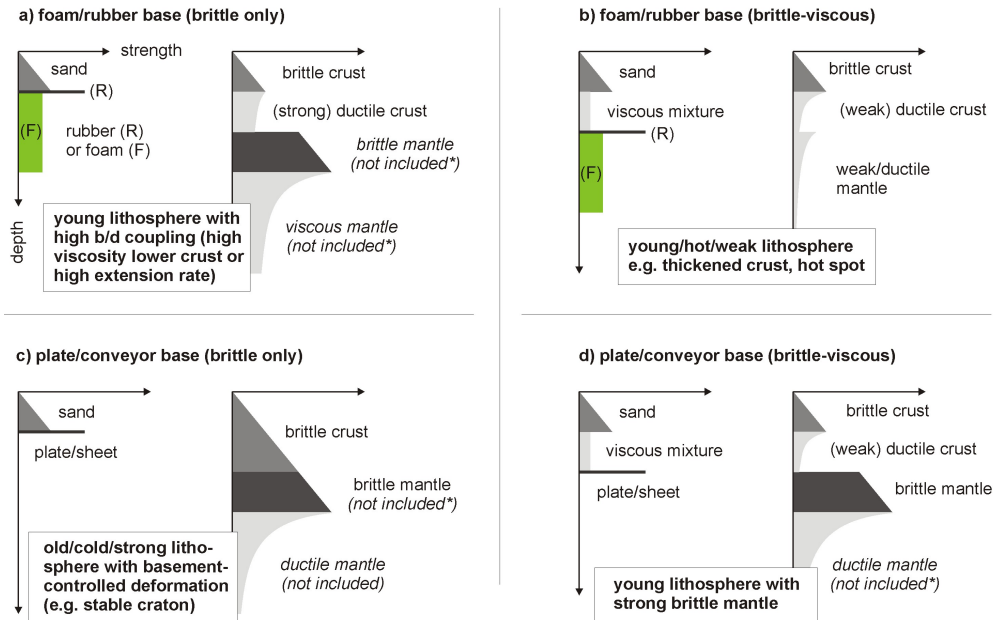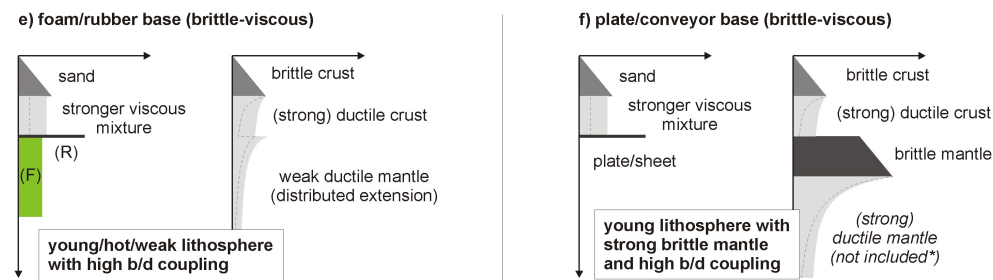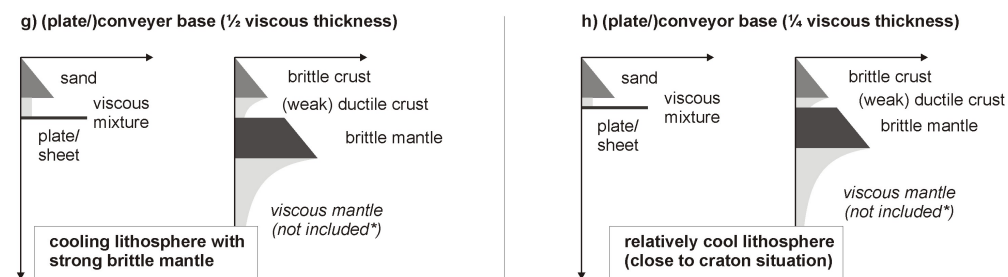
1458
1459
1460  Fig. 3. Schematic experimental and natural strength profiles (always left and right, respectively),
1461  indicating the lithospheric setting that experiments may represent. Dotted lines in (e) and (f)
1462  indicate the strength profile under reference conditions for comparison. (*) the effects of these
1463  layers are not included in the set-up. b/d = brittle/ductile.

1464

**Final top views of brittle-only foam base experiments**
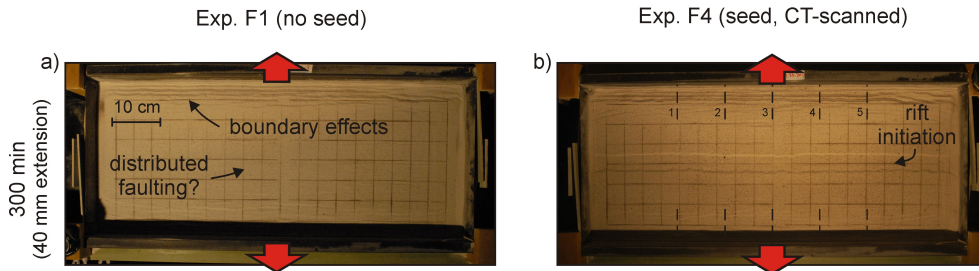
**3D external evolution (Exp. F4)**
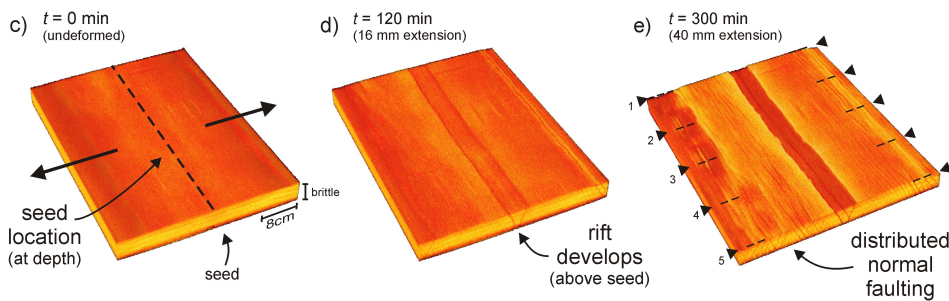
**3D internal evolution (Exp. F4)**
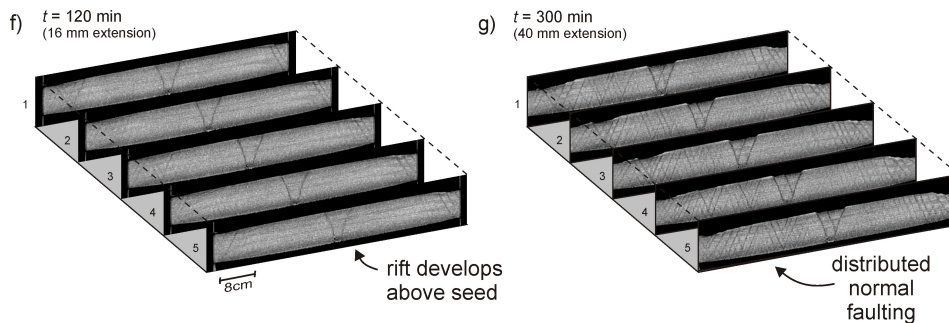
1465
1466
1467    Fig. 4. Foam base (brittle-only) results. (a, b) Top views depicting the final surface structures of
1468    models F1 (no seed) and F4 (with seed). The brittle layer is 4 cm thick and the extension
1469    velocity is 8 mm/h. Note that the boundary effects are present on both sides of the model, but
1470    these are partially invisible due to shadow. (c-d) 3D evolution of CT-scanned model F4. (f, g)
1471    3D internal evolution of CT-scanned model F4.
1472
1473

**Final top views of brittle-viscous foam base experiments**

**3D external evolution (Exp. F7)**

**3D internal evolution (Exp. F7)**
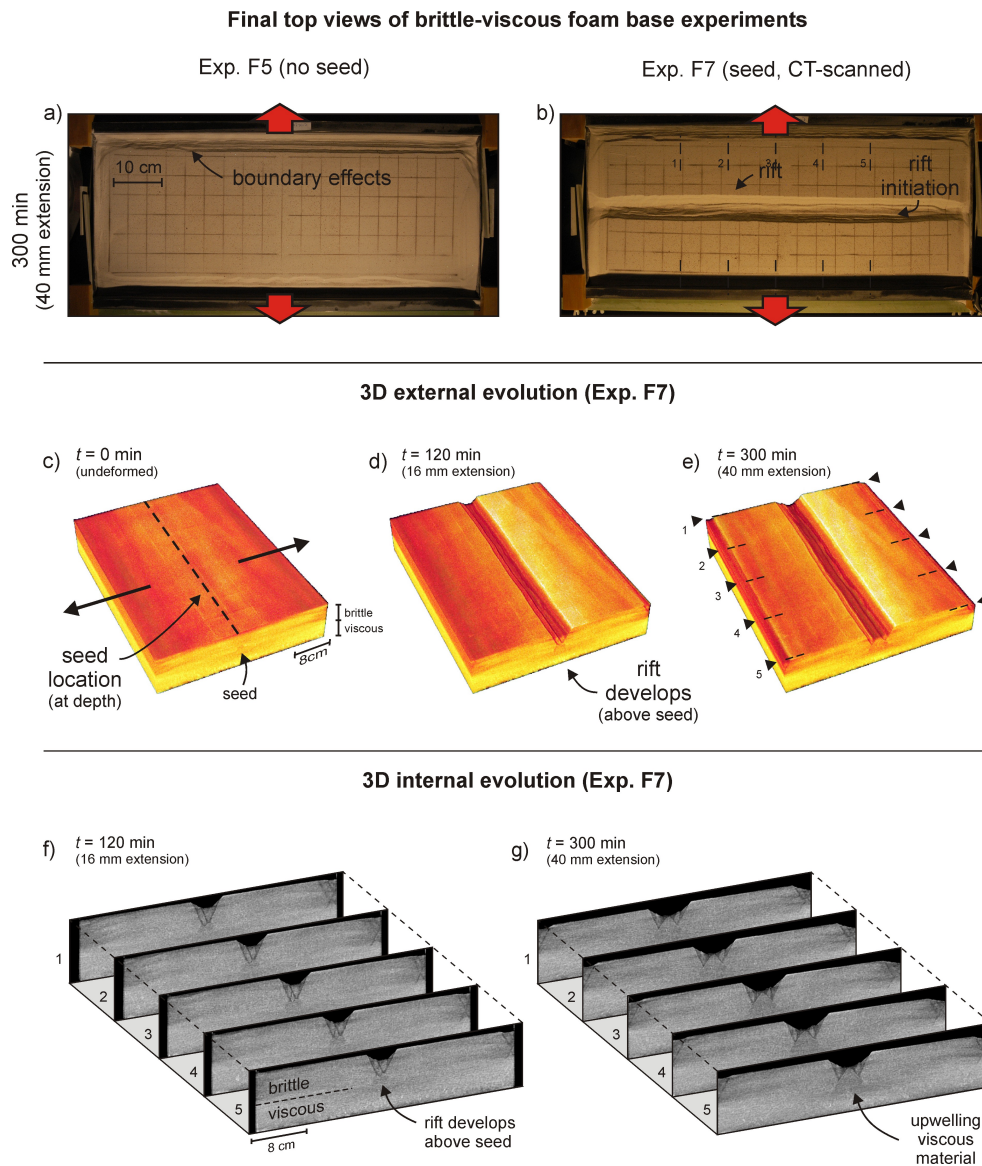
1474
1475
1476  Fig. 5. Foam base (brittle-viscous) results. (a, b) Top views depicting the final surface
1477  structures of experiments F5 (no seed) and F7 (with seed). Both the brittle and viscous layers
1478  are 4 cm thick and the extension velocity is 8 mm/h. Note that the boundary effects are present
1479  on both sides of the model, but these are partially invisible due to shadow. (c-d) 3D evolution of
1480  CT-scanned model F7. (f, g) 3D internal evolution of CT-scanned model F7.
1481
1482
1483
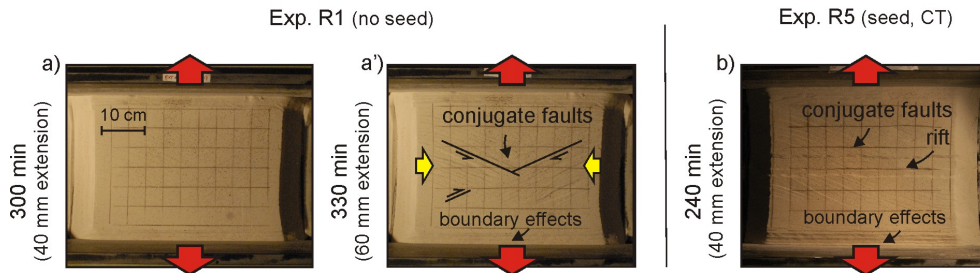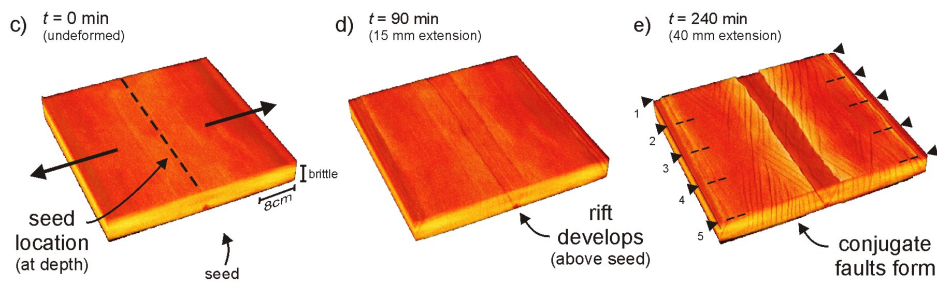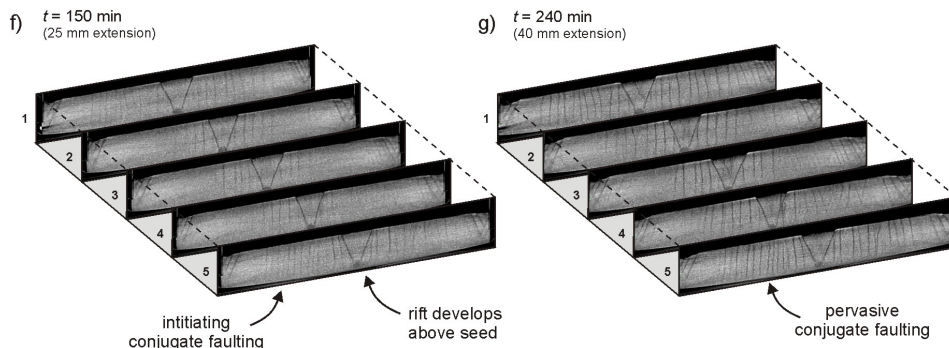
1484
1485
1486 Fig. 6. Rubber base (brittle-only) results. (a, b) Top views depicting surface structures of
1487 experiments R1 (no seed) and R5 (with seed) after 40 mm of extension. Note that (a)
1488 represents the first phase of experiment R1 (8 mm/h), whereas and additional 20 mm of
1489 extension was applied with an enhanced extension velocity of 20 mm/h to amplify structures.
1490 Experiment R5 was run with an extension velocity of 10 mm/h. These deviations from the
1491 reference extension velocity (8 mm/h) are permissible, since the behaviour of sand is time-
1492 independent. The sand layer is 4 cm thick in both experiments. (c-d) 3D evolution of CT-
1493 scanned model R5. (f, g) 3D internal evolution of CT-scanned experiment R5. Note that the
1494 boundary effects are present on both sides of the model, but these are partially invisible due to
1495 shadow.
1496
1497
1498
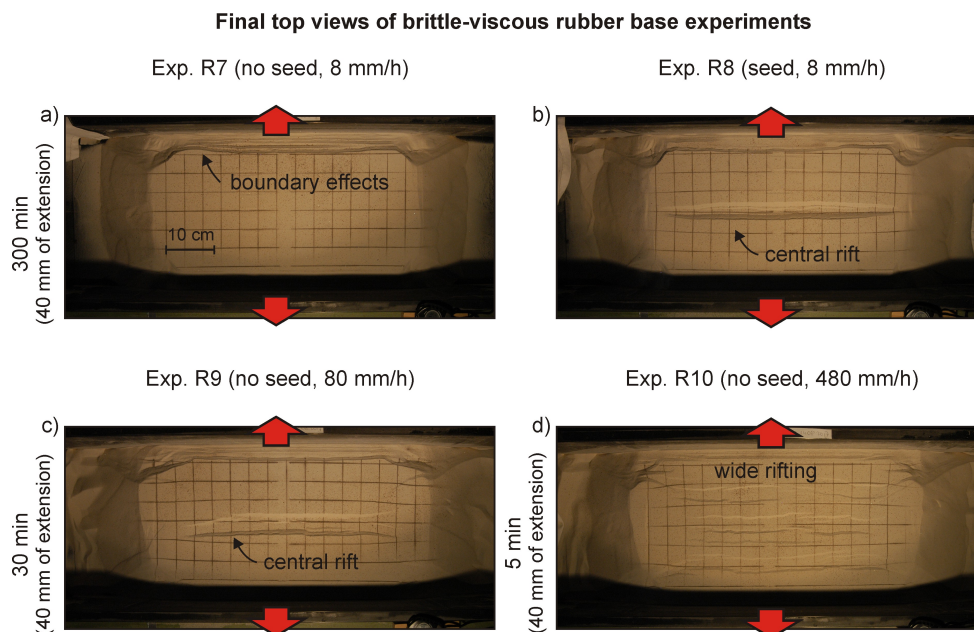
**Final top views of brittle-viscous rubber base experiments**

Fig. 7. Rubber base (brittle-viscous) results. Top views depicting the final surface structures of (a, b) experiments R7 and R8 (reference extension velocity of 8 mm/h) and (c, d) R9 and R10 (high extension velocity experiments: 80 and 480 mm/h, respectively). Note that boundary effects, although partially invisible due to shadow, are present on all sides of the model and therefore especially in the corners.

**Final top views of brittle-only plate base experiments**
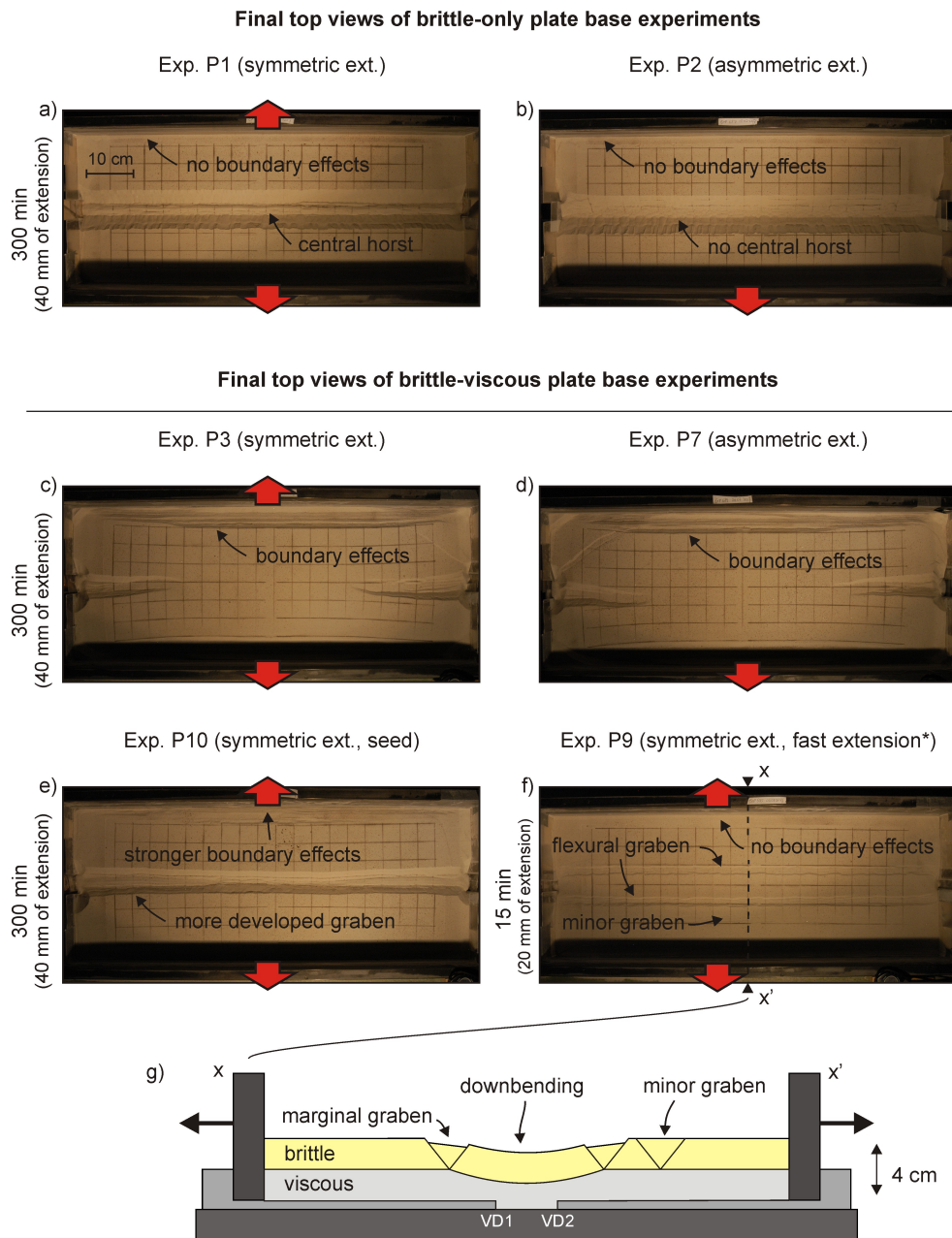
**Final top views of brittle-viscous plate base experiments**

Fig. 8. Overview depicting our plate base results. (a, b) Top views of brittle-only experiments P1 (symmetric extension) and P2 (asymmetric extension). (c-f) Brittle-viscous experiments in map view: (c-d) experiments P3 and P7 (reference extension velocity experiments, without seed), (e) Exp. P10 (reference extension velocity, with seed), (f) Exp. P9 (40 mm total thickness, high extension velocity of 80 mm/h, no seed). Note that boundary effects are present on both sides of the model, but these are partially invisible due to shadow. (g) Schematic section depicting the interpreted internal structures of experiment P9 (high extension velocity experiment) from surface data and the topography of the viscous material after removal of the sand at the end of the model run. Note the two VDs and that the base plates are 3 mm thick

**Final top views of brittle-only coveyor base experiments**

**Final top views of brittle-viscous conveyor base experiments**
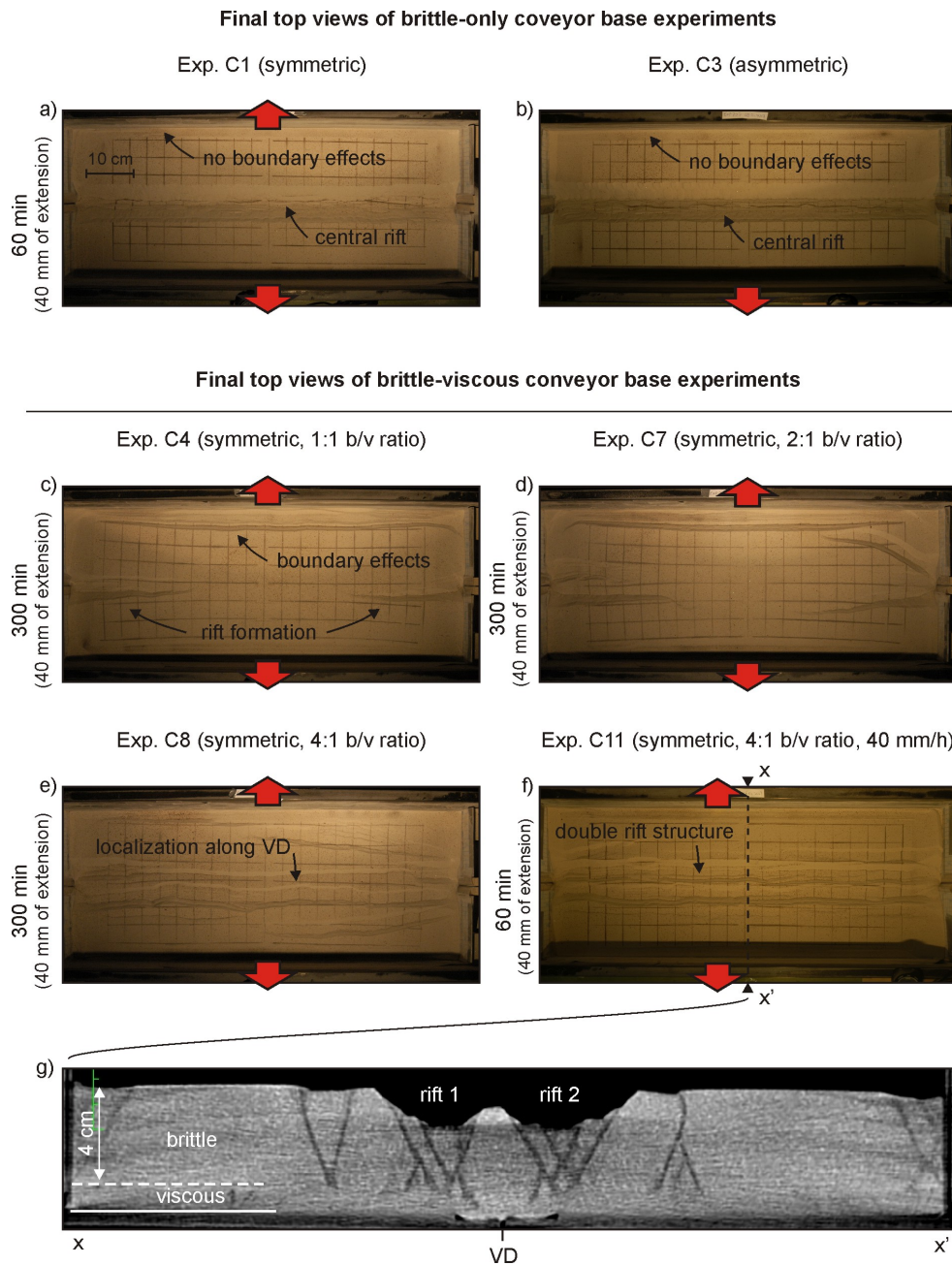
1521
1522
1523 Fig. 9. Overview of conveyor base results. Top views depicting the final surface structures of (a,
1524 b) brittle-only experiments C1 and C3, (c, d) brittle-viscous Exp. C4 (reference layering and
1525 extension velocity), (d) model C7 (reference extension velocity, brittle-to-viscous ratio: 2), (e)
1526 Exp. C8 (reference extension velocity, brittle-to-viscous ratio: 4) and (f) Exp. C11 (elevated
1527 extension velocity: 40mm/h, brittle-to-viscous ratio: 4). Note that the boundary effects (if
1528 present) occur on both sides of the model, but may be partially invisible due to shadow. (g) CT
1529 section depicting the internal structures of Exp. C11.
1530
1531
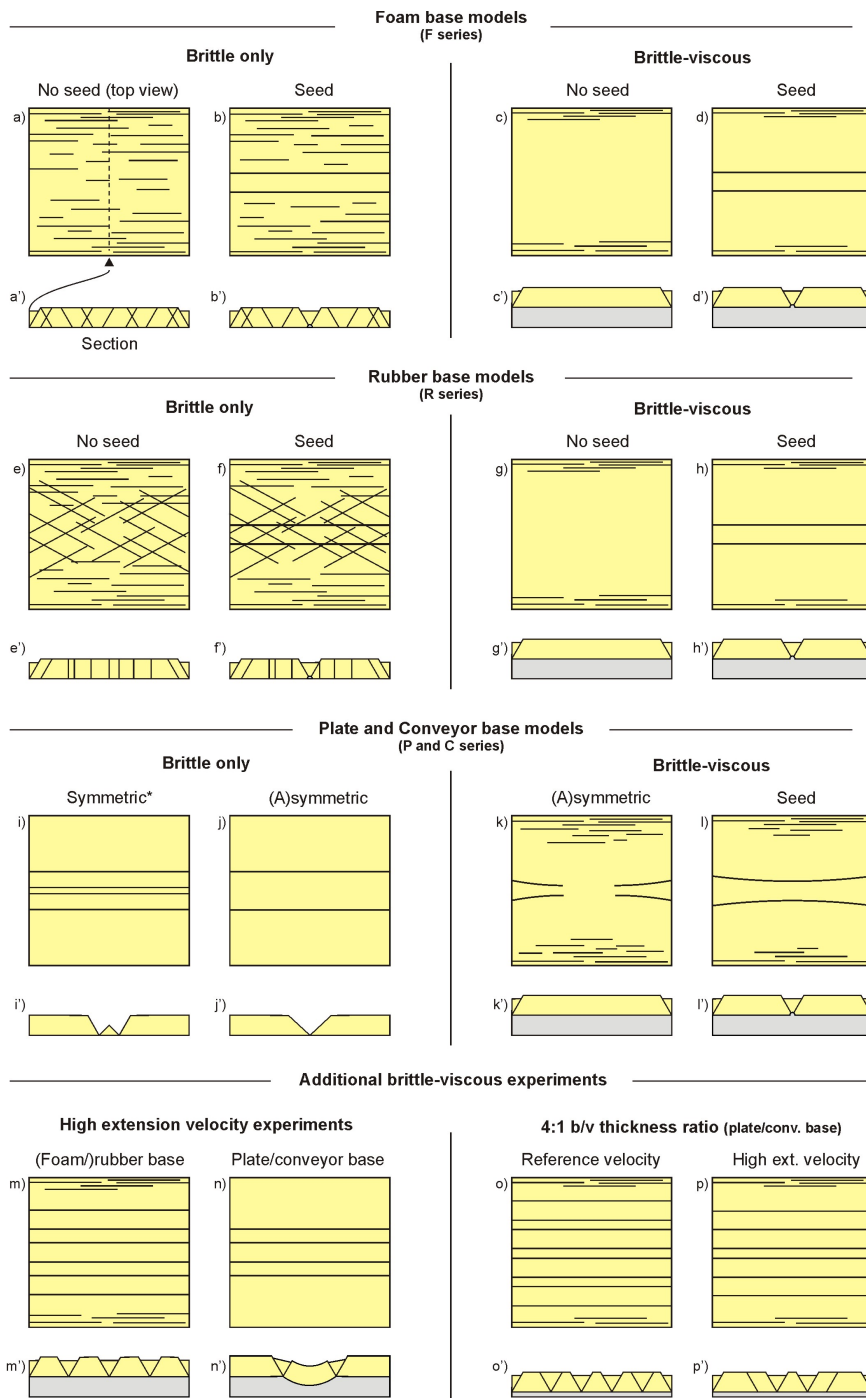
Fig. 10. Schematic summary of our experimental results. (a-l) Experiments with reference brittle-to-viscous ratios (1:1) and reference extension velocities (8 mm/h). (* = plate base model result only). All sections shown go through the central part of the model where boundary effects are minimal. (m-p) Additional brittle-viscous experiments with high extension velocities (80 mm/h) and/or high brittle-to-viscous ratios (4:1).

**Brittle-only examples**

a)  5 cm

rubber base

b)

x  ——  x'

5 cm                section x-x'

rubber base

c)  Symmetric extension

sand

VD
(fixed)

d)  Asymmetric extension

3 cm        fixed        conveyor
            VD

**Brittle-viscous examples**

e)  Rift 1                    Rift 2

sand

silicone

3 cm        moving        base plate
            VD

f)  3 cm

sand        Rift 1          Rift 2

silicone

conveyor sheet 1      conveyor sheet 2
            fixed
            VD

g)  5 cm

sand

silicone

base plate    moving VD
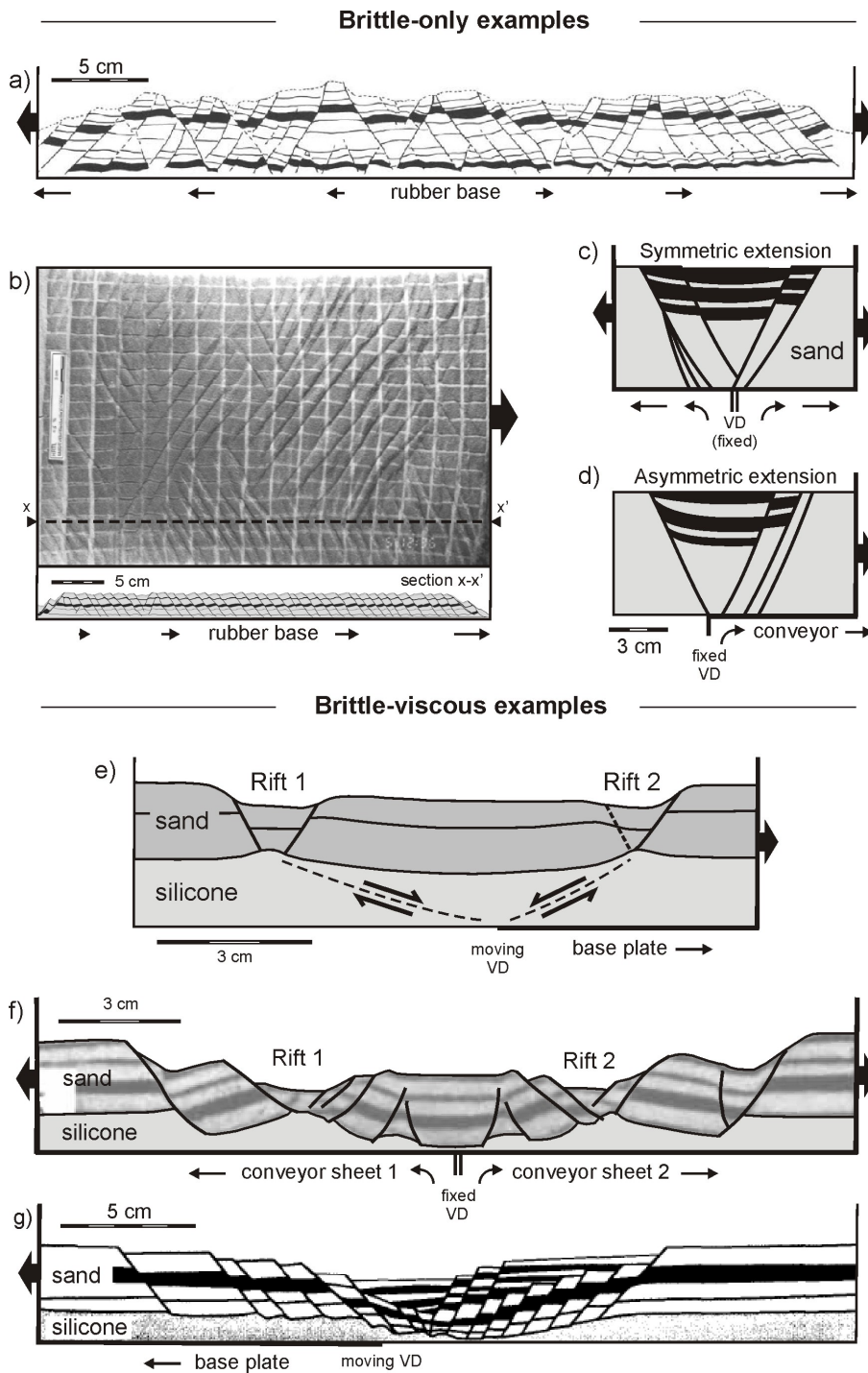
1539
1540
1541
1542
1543

Fig. 11. Examples of previously published analogue models of extensional tectonics. (a) Cross-section of a brittle-only rubber base model, as used for homogeneous thin-skinned deformation. Note the conjugate fault sets. Adapted from Vendeville et al. (1987) with permission from the Geological Society, London. (b) Top view and cross-section of a brittle-only rubber base model similar to (a), although developing the conjugate fault sets due to extension-perpendicular contraction of the rubber sheet (Poisson effect). Adapted from Bahroudi et al. (2003) with permission from Elsevier. (c-d) Cross-sections of brittle-only conveyor base experiments with symmetric (c) or symmetrical extension (d), both including syn-rift sedimentation. Here the VD may represent a basement structure controlling deformation in the overlying strata. Redrawn after Allemand & Brun (1991) with permission from. (e-g) Cross-sections of brittle-viscous models with a plate base or conveyor belt set-up, with the VD representing a fracture in the strong brittle mantle affecting the overlying crustal analogues. (e) Brittle-viscous plate base model with asymmetric extension, illustrating the relation between the velocity discontinuity (VD) and the two rift basins. Compare with model C11 (Figs. 9f, g, B2). Redrawn (with permission from Elsevier) after Michon & Merle (2003), who investigated the European Cenozoic Rift System and the influence of VDs in a strong upper lithospheric mantle. (f) Symmetric extension model with conveyor set-up and brittle-viscous layering, designed to simulate the influence of a strong mantle on a two-layer crust. Adapted from Tron & Brun (1991) with permission from Elsevier. (g) Brittle-viscous plate base model with asymmetric extension. Note that this experiment includes syn-rift sedimentation and aims to reproduce the North Sea Viking Graben. Modified after Brun & Tron with permission from Elsevier (1993). Black arrows indicate extensional motion. VD: velocity discontinuity.
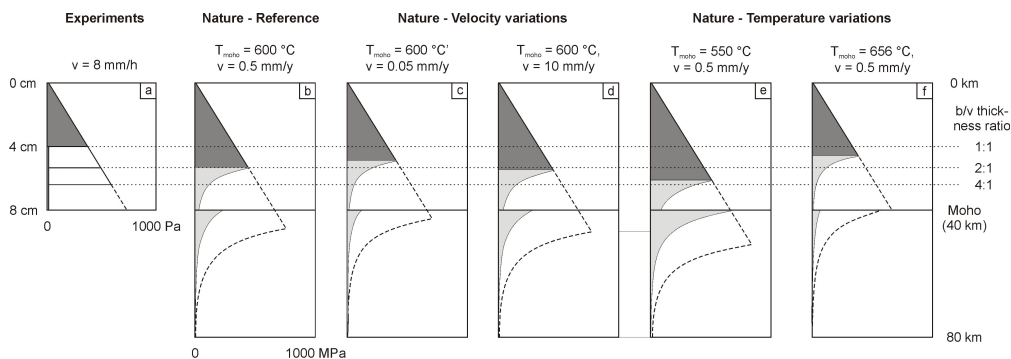
Fig. 12. Strength profiles calculated for our experiments (a) and various natural cases (b-f). Reference values for the natural example are $T_{moho}$ = 600 °C and v = 0.5 mm/y (b). Extension velocity variations are shown in (c) and (d) and variations due to different Moho temperatures are depicted in (e) and (f). The crust and mantle flow laws used here are anorthosite dislocation creep (Rybacki et al. 2006) and olivine dislocation creep (Hirth & Kohlstedt 2003). Note that the filled-in profile represents a wet lithosphere, whereas the dotted profiles delineate a dry lithosphere scenario. The horizontal lines indicate various brittle-to viscous ratios (see discussion in text).

1583 **Appendix Figures**
1584
1585
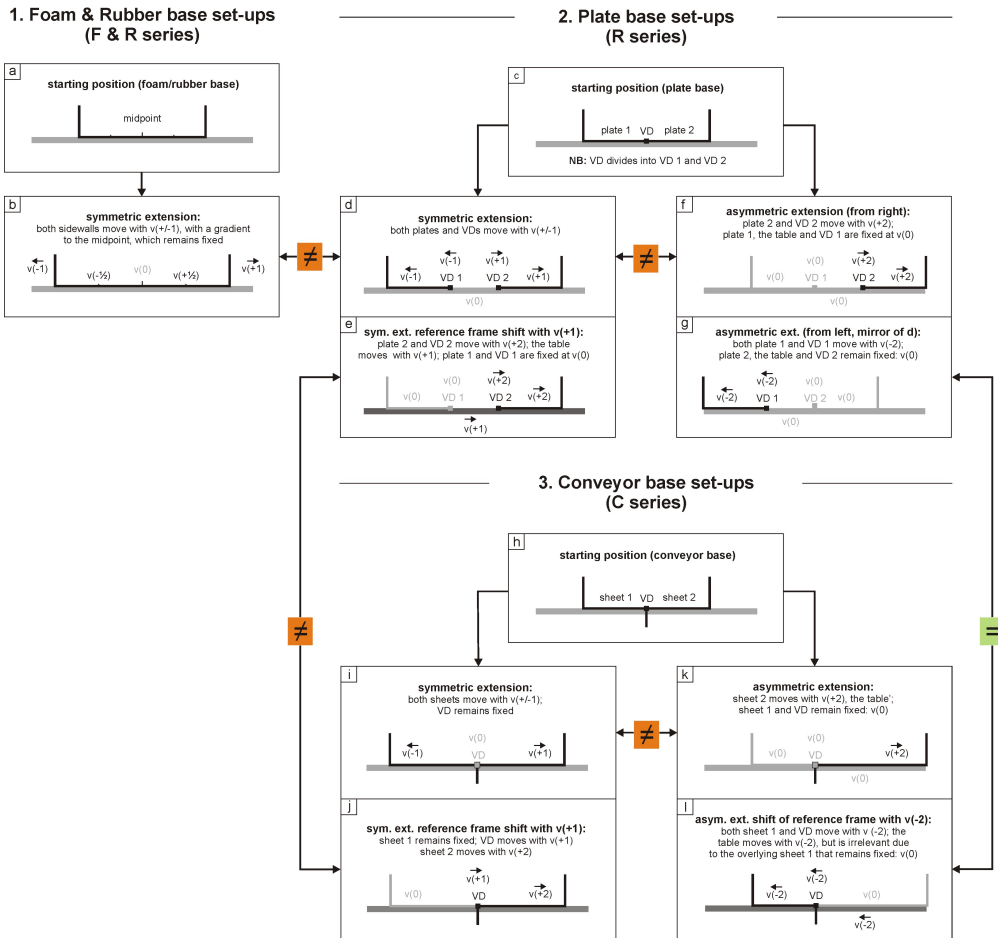
1586
1587
1588 Fig. A1. Schematic overview of relations between experimental set-ups, illustrated with shifts of
1589 reference frame (v = velocity, VD = velocity discontinuity). Compare with Fig. 2. (a-b)
1590 Foam/rubber base set-ups, in which the base induces a extension gradient. (c-g) Plate base
1591 set-ups. (h-l) conveyor base models. Shifts of reference frame are used to highlight the direct
1592 differences between models. Note that most set-ups fundamentally differ as indicated by the (≠)
1593 sign, except for the asymmetric plate base and conveyor base set-ups (f-g, k-l), which are
1594 fundamentally the same. The latter are indicated by the (=) sign. Darker colors indicate mobile
1595 parts of the set-ups, whereas brighter colors indicate static parts.
1596
1597

Brittle-only foam base (with seed)  Brittle-viscous plate base (no seed)

Brittle-viscous foam base (with seed)

Brittle-viscous conveyor base (no seed)
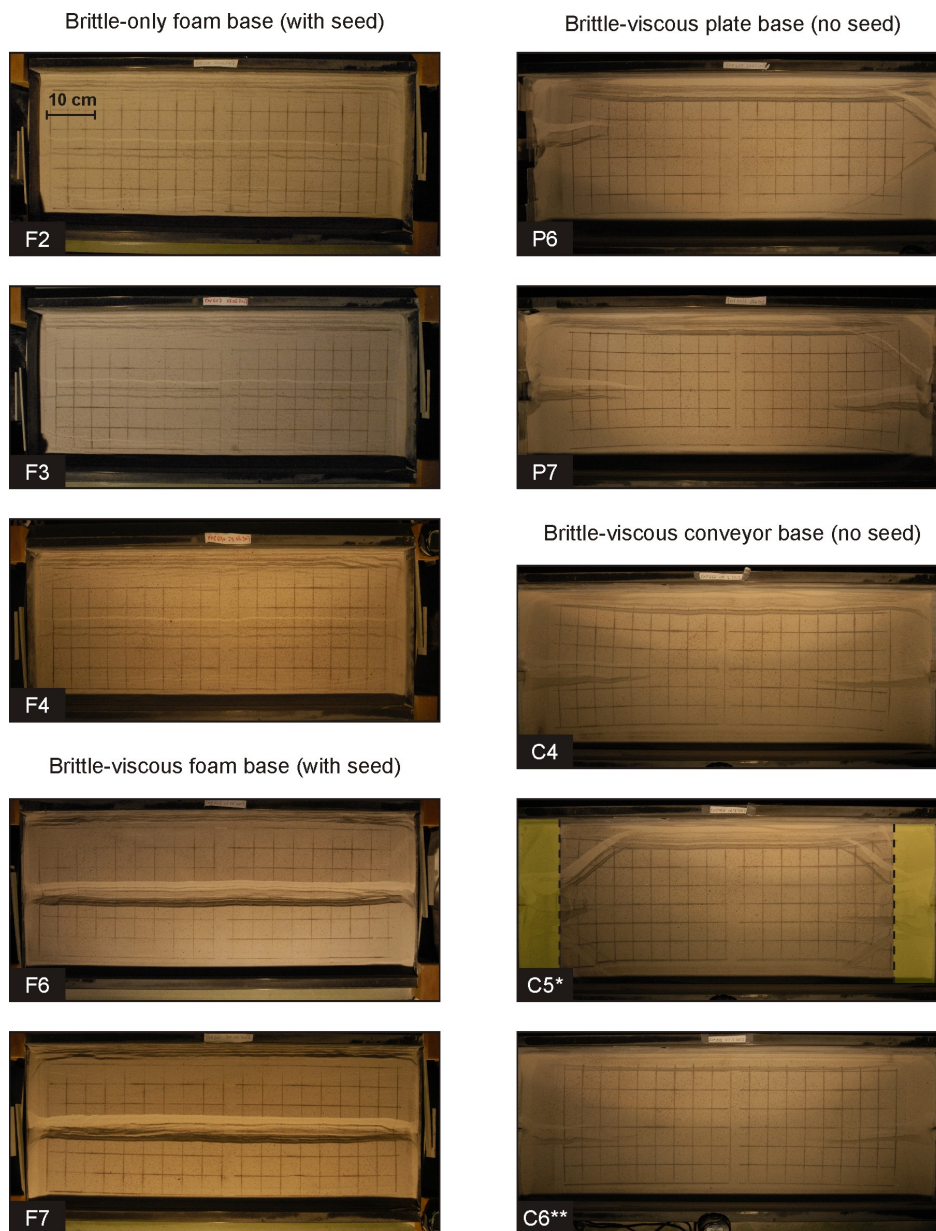
1598
1599
1600 Fig. B1. Reproducibility tests. Final top views of experiments F2-F4 (brittle-only, foam base,
1601 with seed), F6 and F7 (brittle-viscous foam base, with seed), P6 and P7 (brittle-viscous plate
1602 base models, no seed) and C4-C6 (brittle-viscous conveyor base, no seed). Note that C5* and
1603 C6** were attempts to decrease boundary effects by replacing part of the basal viscous layer
1604 with sand (transparent overlay) or adding a lubricant (hand soap) along the short ends of the
1605 set-up, respectively. The former however increased boundary effects, whereas the latter did not
1606 significantly change surface structures and was therefore halted after 2 hours. Extension
1607 velocities are 8 mm/h in all cases.
1608
1609
1610

Brittle-only asymmetrc plate/conveyor base    Brittle-visc. conv. base (4:1 b/v ratio, high v)

Brittle-viscous plate/conveyor base (high velocity)
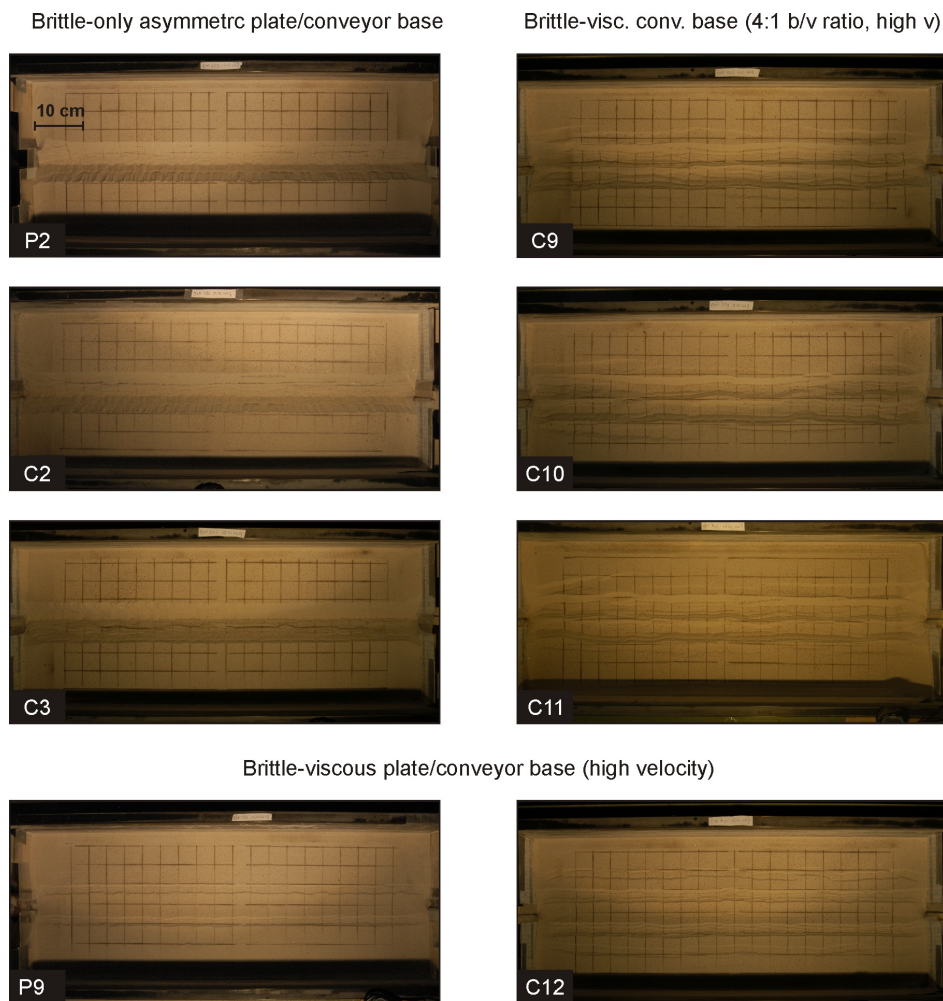
Fig. B2. Reproducibility tests. Final top views of experiments P2, C2 and C3 (brittle-only asymmetric plate base [P] and conveyor base [C]), C9-C11 (brittle-viscous conveyor base models, 4:1 brittle-viscous thickness ratio, high velocity: 40 mm/h [C10/C11] and 80 mm/h [C9]) and experiments P9 and C12 (brittle-viscous plate base [P] and conveyor base [C], half layer thickness, high extension velocity: 80 mm/h).